COMPUTER SCIENCE

Generic generation of noise-driven chaos in stochastic time delay systems: Bridging the gap with high-end simulations

Mickaël D. Chekroun[1,2]*, Ilan Koren[1], Honghu Liu[3], Huan Liu[1]

Nonlinear time delay systems produce inherently delay-induced periodic oscillations, which are, however, too idealistic compared to observations. We exhibit a unified stochastic framework to systematically rectify such oscillations into oscillatory patterns with enriched temporal variabilities through generic, nonlinear responses to stochastic perturbations. Two paradigms of noise-driven chaos in high dimension are identified, fundamentally different from chaos triggered by parameter-space noise. Noteworthy is a low-dimensional stretch-and-fold mechanism, leading to stochastic strange attractors exhibiting horseshoe-like structures mirroring turbulent transport of passive tracers. The other is high-dimensional , with noise acting along the critical eigendirection and transmitted to "deeper" stable modes through nonlinearity, leading to stochastic attractors exhibiting swarm-like behaviors with power-law and scale break properties. The theory is applied to cloud delay models to parameterize missing physics such as intermittent rain and Lagrangian turbulent effects. The stochastically rectified model reproduces with fidelity complex temporal variabilities of open-cell oscillations exhibited by high-end cloud simulations.

INTRODUCTION

Among the various mechanisms of generation of chaos for low-dimensional systems, the phenomenon of shear-induced chaos, known perhaps since the work of van der Pol and van der Mark (*1*) (reported as "irregular noise" at that time), has gained a lot of attention and new insights in recent years as led by Young and collaborators (*2*). Stated in simple terms, shear-induced chaos is characterized by complex geometric structures in the state space associated with stretching and folding caused by the interactions between suitable time-dependent perturbations or noise with nonlinear oscillations (*2*). The key idea behind it is that for a nonlinear system exhibiting an attracting limit cycle, Γ, not all the points near Γ in the state space X respond the same way to random, nonuniformly distributed perturbations F. Because of nonlinear effects, the relaxation toward Γ is not uniform, and angular velocities may vary substantially from "within" to "outside" of the limit cycle, causing "shear" effects in the vicinity of Γ that manifest as stretch-and-fold deformations in X when F is applied in the course of time. Convenient ways to reveal such a phenomenon consist of either adopting the viewpoint of Poincaré return maps (*3*) or that of pullback attractors (PBAs) closely related to the notion of snapshot attractors (*4*, *5*).

Within either framework, it can be rigorously established that when suitably perturbed by a time-dependent forcing, a limit cycle can be turned into a strange (pullback) attractor [see theorem 1 in (*6*)]. At the core of this "strangenessfication" of a limit cycle is a geometric mechanism for the production of chaos with simple and intuitive conditions that were first mathematically framed by Wang and Young (*7*) and generalized in subsequent works of the same authors (*6*, *8*) while applied in several applications such as in laser dynamics (*9*) or neuron models (*10*, *11*). Loosely speaking, in the case of a steady-state losing its stability via a supercritical Hopf bifurcation, if the stable foliation of the bifurcated limit cycle has its curves sufficiently twisted, then suitable periodic or random kicks (*12*) in the vicinity of the limit cycle lead to folding and stretching of the phase space and, eventually, to the emergence of a strange PBA.

The emergence of strange attractors that result from such stretch-and-fold actions has also been addressed rigorously for periodically forced or randomly kicked infinite-dimensional dynamical systems by Lu *et al.* (*13*), covering the case of systems of parabolic partial differential equations (PDEs). However, because of difficulties inherent with high dimensions, the efficient production of such noise-driven chaos has been poorly documented on a numerical ground. Furthermore, the results of (*13*) do not readily translate to time delay systems, which constitute another class of infinite-dimensional models of prime relevance in many applications. Time delay systems arise in diverse fields of biology (*14*, *15*), neurobiology (*16*), social systems (*17*), semiconductor lasers (*18*), and climate dynamics (*19*–*21*), to name a few. Intuitively, the use of delay terms allows for describing many natural processes in a compact and physically intuitive manner. The delay term can be the outcome of competing processes with a noninstantaneous response yielding a phase shift. In essence, many predator-prey–like systems would have a characteristic delay.

It is hence without surprise that time delay systems produce generically nonlinear periodic oscillations caused by delay effects [chapter 2 in (*22*)]. The study of emergence of chaotic behavior in deterministic and unforced time delay systems arising typically through diverse bifurcation scenarios has been abundantly documented in the literature [see, e.g., (*23*, *24*) and references therein]. Chaos produced by periodic forcing applied to time delay systems has also attracted attention over the recent years [see, e.g., (*20*, *25*)]. Yet, many questions remain regarding the emergence of chaos in

[1]Department of Earth and Planetary Sciences, Weizmann Institute of Science, Rehovot 76100, Israel. [2]Department of Atmospheric and Oceanic Sciences, University of California, Los Angeles, Los Angeles, CA 90095, USA. [3]Department of Mathematics, Virginia Tech, Blacksburg, VA 24061, USA.
*Corresponding author. Email: michael-david.chekroun@weizmann.ac.il

forced-dissipative systems, with delays, especially regarding the occurrence of noise-driven chaos resulting from the interplay between noise and delay effects. We emphasize that we are not after noise-induced chaos that would be excited by random fluctuations igniting a chaotic motion nearby the periodic motion in the parameter space. Rather, we are after understanding the conditions for the production of shear-induced chaos resulting from noise′s action on periodic motion in time delay systems and the system′s temporal response in view of applications. By the generic character of periodic solutions produced by time delay systems (*22*, *26*), the question of prediction of this noise-driven chaos is potentially of wide interest although yet unanswered.

It is the purpose of this article to fill this gap. Our goal is thus to develop a general understanding for the production of noise-driven chaos caused by stretch-and-fold actions resulting from the interactions of suitable stochastic perturbations with delay-induced periodic oscillations. We pursue here not only to push the generation of noise-driven chaos to the realm of nonlinear time delay systems with infinitely many degrees of freedom but also to address the inherent computational and implementation aspects in view of an efficient prediction of the corresponding dynamical behaviors.

The task is challenging, but its resolution is potentially valuable for many applications. In that respect, we demonstrate the main ideas on a cloud physics problem, which provides a natural ground for the introduction of fast, small-scale, random fluctuations that would be originated from microphysics or other subgrid-scale processes (turbulence) [see, e.g., (*27*, *28*)]. Within a broader perspective, the introduction of parameterization of unresolved scales is often sought to provide closure models. These are aimed at faithfully emulating the dynamics of the macroscale variables, but the design and effects of these parameterizations advocated on a stochastic ground over the recent years (*29*) are often poorly understood on a nonlinear dynamics ground. Thus, to advance the understanding about the emergence and characterization of complex dynamics resulting from the interactions between stochastic perturbations and nonlinear effects constitutes a question with a growing and practical interest in the contemporary modeling of complex systems.

In parallel, the introduction of delay mechanisms in cloud physics was proposed by Koren and Feingold (KF) in (*30*) to describe large-scale patterns formed in shallow marine clouds. Through lagged effects that represent the autoconversion of the small droplets into rain drops by collision coalescence processes, they suggested that the transition between closed to open cellular convection observed in marine clouds can be interpreted as the states of nonlinear oscillations that are driven by these lagged effects. Either in the original KF model or its simplification known as the Koren-Tziperman-Feingold (KTF) model (*31*), such delay-induced nonlinear oscillations were shown to arise through a Hopf bifurcation scenario (*32*). Such conceptual modeling approaches are concerned with the representation of emergent properties of the system rather than detailed interactions between its components. It seeks simple governing mechanisms that are the product of the various processes and feedbacks involved without representing them in full detail. This system′s macroscale view is informative as it points out to emergent solutions that can be potentially confronted to observations and more complex models such as detailed large eddy simulations (LES) (*33*, *34*).

Nevertheless, the delay-induced periodic oscillations obtained with such delay models are too idealistic compared to satellite observations of open-cell oscillations (*35*), and this is where the mathematical question of this study meets our physical motivations: Can one rectify these periodic oscillations obtained from delay models toward more realistic ones by the action of fast, stochastic perturbations? In other words, can irregular open-cell oscillations be explained in dynamical terms by means of stochastic perturbations (such as, e.g., caused by microphysics/subgrid-scale processes) interacting with periodic solutions naturally caused by delay effects? For that purpose, we focus on the KTF delay model (*31*), but as it will become apparent below, our findings apply to a broad class of delay differential equation (DDE) models that could thus benefit other fields of applications.

By combining recent reduced-order modeling techniques for delay models of (*32*), with the recent advances in the understanding of the phenomenon of shear-induced chaos (*2*), we answer positively the questions raised above. In particular, we show that irregular but recurrent oscillations may be produced systematically out of suitable stochastic perturbations of delay-induced nonlinear oscillations and that such oscillations are associated with stochastic attractors evoking Smale′s horseshoe structures (*36*, *37*).

To understand the production of such oscillations and structures, we first recall in the "Noise-driven chaos from delay models" section the geometric mechanisms at play for the production of shear-induced chaos out of time-dependent perturbations of planar systems. Here, the design problem of such perturbations is solved in the case of a weak shear near the limit cycle, such as encountered for the Hopf normal form of the KTF model analyzed in this article. We deal then with the practical design of these perturbations for the effective production of stochastic strange attractors exhibiting stretching and folding for the underlying stochastic transport problems. These transport problems are central for the generation of stochastically rectified DDE solutions. Complementary to such noise-driven chaos reminiscent to that of passively advected particles in a turbulent fluid flow, we also identify a completely different type of noise-driven chaos that resembles that of a swarm-like behavior of starlings, i.e., of amurmuration phenomenon (*38*).

Unlike the horseshoes case, the murmuration chaos does not result from low-dimensional dynamical mechanisms and cannot be predicted from the Hopf normal form anymore. Rather, the noise acting along the critical eigendirection, and thus low dimensional, is transmitted through the nonlinear terms to the vast number of unforced scales, leading to notable power-law and scale break properties of the dynamics. The response to stochastic parameterization is then analyzed in further details, particularly regarding the frequency content of the noise-driven solutions and its dynamical origin. Last, we show in the "Comparison with high-end simulations" section that the insights gained from the theory enables us to stochastically rectify the KTF limit cycle into solutions that reproduce with fidelity complex temporal variabilities of open-cell oscillations exhibited by high-end cloud simulations. There, the stochastic perturbations account for intermittent rain production and turbulent Lagrangian effects not initially included in the KTF model. We summarize lastly the results and point out to other applications in Discussion.

RESULTS

High-end simulations of cloud fields

To better substantiate the questioning we are after, we report briefly on a real-world case study of a cloud field exhibiting both open and closed cellular cells, which will serve below to benchmark our noise-driven approach aimed at rectifying delay-induced period oscillations (from the KTF model) toward more realistic ones. This cloud field took form on 18 January 2020 during a cold air outbreak with a mid-latitude cyclone developed over the western North Atlantic Ocean. The remarkable open- and closed-cell structures are shown in Fig. 1A from the cloud's reflectance as retrieved from the satellite GOES-16 channel 2 (0.65 μm) radiance with a nadir horizontal resolution of 500 m (*39*).

Often the observations of such a cloud field exhibit complicated spatio-temporal oscillations that are difficult to apprehend. An important step for their analysis has been taken in (*35*) in which a Lagrangian tracking method has been introduced to filter out the atmospheric advective effects to isolate the clouds' self-organized oscillations. This approach allows for revealing spatially and temporally oscillating cloud patterns as well as quasi-stationary state cloud patterns associated, respectively, with open and closed cells. Such features are in qualitative, "metaphored" agreement with the Hopf bifurcation as exhibited by the KF and KTF delay models (*31*, *32*). As pointed out in Introduction, the underlying delay-induced oscillations produced through this bifurcation are, however, too idealistic (since periodic) to represent faithfully the oscillations' complexity as manifested from satellite observations. Nevertheless, despite their periodic solutions, such conceptual delay models have been credited recently a certain ability to produce a range of (periodic) oscillations that share similarities when compared to filtered cycles of cloud growth and decay as extracted from LES (*40*). To do so, the diversity of the KTF periodic solutions in the parameter space is constrained by the LES outputs using parameter estimation techniques.

In this work, our approach is radically different. We are interested in producing diversity in the KTF model's response to stochastic perturbations mimicking the missing physics (e.g., parameterization) without constraints against any LES output. Rather, our goal is to identify the intrinsic, nonlinear mechanisms enabling these perturbations to turn KTF periodic cycles into solutions with a rich frequency content and amplitude modulations that resemble open-cell oscillations as observed in nature and simulated by high-end models of cloud physics.

The high-end model retained for this purpose is the Weather Research and Forecasting (WRF) model, which is a state-of-the-art mesoscale numerical weather prediction system designed for both atmospheric research and operational forecasting applications (*41*). The WRF run conducted here is aimed at reproducing the physical variables underlying the satellite observations shown in Fig. 1A (see Methods for more details). Figure 1 (B and C) shows the vertical velocity just below the clouds base (~750 m) at the same specific time (20 January 18, UTC 12:40:00) for the regions delimited by the red and blue boxes shown in Fig. 1A, respectively. These boxes evolve in time and follow a Lagrangian path that filters out the background advection and that hence enables us to extract the intrinsic open-cell and closed-cell dynamics (*35*) over the tracked domains. The closed cellular state is a mostly cloudy state characterized by broad, weak updrafts in the opaque cloudy cell center and stronger, narrower downdrafts around the cell edges. The open-cell state is the "polar opposite" or "negative" in which narrow, strong, cloudy updrafts surround broad, weak downdrafts in the optically thin cell center. The simulated vertical velocity field reconstructs these features almost perfectly: The cloudless open-cell centers are associated with downdrafts, while the cloudy open-cell boundaries are associated with updrafts (Fig. 1B) and just the opposite for the

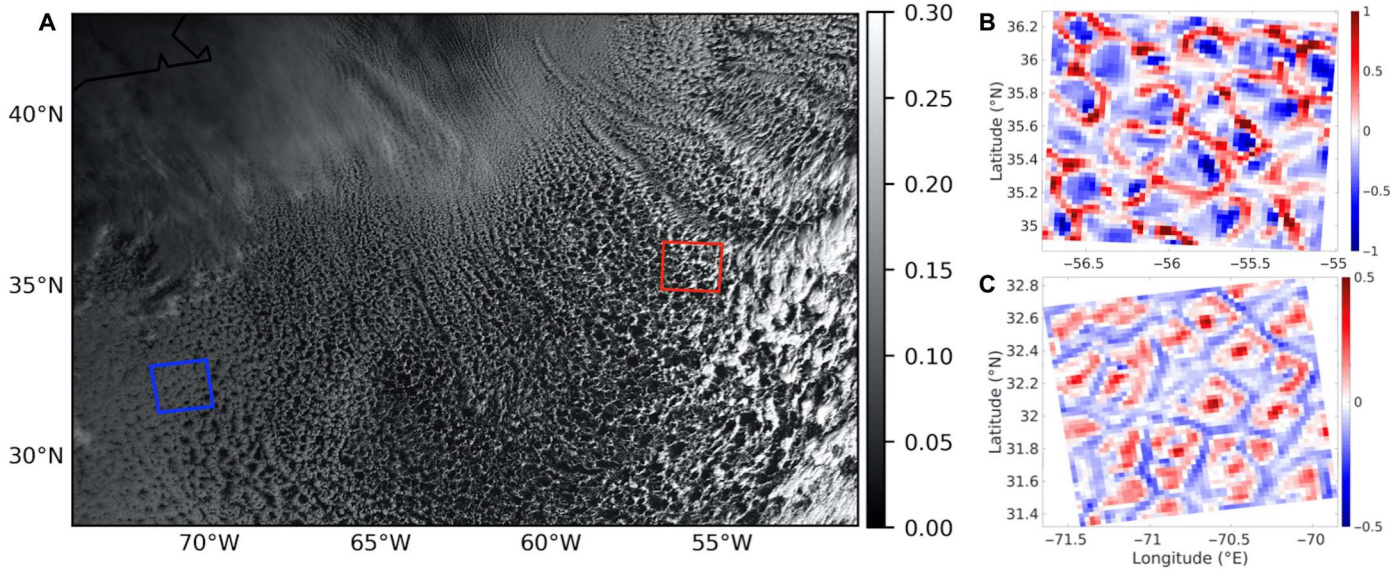

Fig. 1. Open-cell and closed-cell fields: Satellite observation and high-end simulations. (**A**) Open- and closed-cell structures from the cloud's reflectance as retrieved from the GOES-16 channel 2 (0.65 μm) radiance with a nadir horizontal resolution of 500 m. (**B**) and (**C**) show results from the simulation (vertical velocity at ~750 m is shown) of the WRF model and correspond to the blue and red boxes shown, respectively, in (A). (B) [resp. (C)] displays open-cell (resp. closed-cell) patterns. Transitions from closed-cell patterns to open cell ones are visible from west to east over a zonal strip in the latitude range (28°N,36°N). See fig. S10 for a high-fidelity WRF simulation of the cloud field shown in (A) from which (B) and (C) are extracted.

closed cellular cells (Fig. 1C) (see fig. S10 for a WRF simulation over the whole domain as shown in Fig. 1A).

The comparison between KTF model's response to stochastic perturbations and WRF time series is discussed at the end of this article, in the "Comparison with high-end simulations" section. We turn next to the nonlinear mechanisms at the core of the transformation of KTF periodic cycles into noise-driven solutions with a rich frequency content obtained by means of well-designed stochastic perturbations.

Noise-driven chaos from delay models

Stretching and folding nonlinear oscillations from noise

Before dealing with the production of noise-driven chaos out of stochastic perturbations of nonlinear oscillations issued from DDE models, we recall below the geometric mechanisms at play in the case of planar systems. At the core of these mechanisms lies the notion of isochron (iso, equal; chronos, time, in Greek) that was introduced by Winfree (*42*) in his seminal work to address timing relations in oscillators perturbed off their attracting cycles. Winfree showed that to understand the response to elemental perturbations boils down to understanding the functional dependence of the phase on the state. This functional dependence is captured by the isochrons, which provide the sets of phase-equivalent initial conditions in the state space that lead to rhythms that are synchronous in asymptotic time [box B, page 167 in (*43*)].

More precisely, given an attractive limit cycle Γ, whose orbit is $u(t)$, recall that the asymptotic (or latent) phase of a point x_0 in the basin of attraction of Γ is the scalar $\varphi(x_0)$ for which

$$\lim_{t\to\infty} \| x(t) - u(t+\varphi(x_0)) \| = 0 \tag{1}$$

where $x(t)$ is the trajectory starting at x_0 off Γ [see, e.g., chapter 13, theorem 2.2 in (*44*)]. Then, the locus of all points sharing the same asymptotic phase $\varphi(x_0)$ is called an isochron. In other words, the isochrons are interpreted as the level sets of the phase function φ. These isochrons form also the curves constituting the stable foliation of the limit cycle (*45*) (see Methods). They provide a global picture of the nonlinear dynamics associated with a limit cycle and organize the response to localized perturbations such as spikes (*11*, *43*, *46*).

The isochrons and, particularly, their twist (or bending) also provide the key elements to understand the mechanisms at play for generating chaos by exerting upon a limit cycle more general time-dependent forcing, possibly stochastic (*2*, *9*, *12*, *47*). In the case of the Hopf normal form, $\dot{z} = (a+ib)z - (\alpha+i\beta)z|\ z\ |^2$, the isochrons' twist is controlled by the ratio β/α; the larger it is, the more auspicious it is for noise-driven chaos to take place—characterized by a strange PBA emerging from stochastic perturbations of a limit cycle (*2*, *48*). In this case, points in the complex plane rotate with different angular speed depending on their distance from the origin, and intuitively, applications of random kicks, nonuniformly distributed in time and in space, lead to different system's responses, which may lead to erratic, chaotic behaviors. On the other hand, when the twist parameter β/α is small enough, then depending on the noise intensity, the top Lyapunov exponent becomes strictly negative and the random PBA reduces to a random fixed point [see theorems B and C in (*48*)]. More details are provided in the "Smale's horseshoes from normal form: Noise design" section.

Thus, as the system is suitably kicked in both radial and angular directions, competing in an appropriate balance with the nonlinear relaxation toward the unkicked system's limit cycle, a series of stretch-and-fold actions may result from this interplay between the kicks and the local state space's geometry. These stretch-and-fold actions—if sufficiently frequent in the course of time—lead eventually to the creation of Smale's horseshoes (*2*), i.e., (hyperbolic) chaotic dynamics (*36*, *49*). Depending on the degree of isochrons' twist, the kick does not have to be so specific or carefully chosen. It may be sufficient to kick nonuniformly in the radial direction alone and rely on natural forces of nonlinear shear to provide the necessary stretch-and-fold actions. This is, however, not the case for the Hopf normal form issued from the DDE model considered next, requiring the perturbations to somehow enhance the isochrons' twist as explained below.

Smale's horseshoes from normal form: Noise design

We turn now to the generation problem of noise-driven, Smale's horseshoe-like structures from DDE models. To serve as an illustration, we consider the following KTF model from cloud dynamics

$$\dot{h} = 1 + ah(t) - bh^2(t-\tau), \tau > 0 \tag{2}$$

in which $a = -1$ and $b = \frac{1}{\mu}$ ($\mu > 0$), while the variable h represents the (normalized) cloud height. In this conceptual model, the delay parameter τ is a key parameter that controls the time it takes from the onset of droplet coalescence to the rain sedimentation and thus the dynamical regimes' bifurcations (*31*, *32*). For this choice of a and b, Eq. 2 admits only one physically relevant steady state given by $\bar{h} = (-\mu + \sqrt{\mu^2+4\mu})/2$. The KTF model (Eq. 2) rewritten for the perturbed variable, $H(t) = h(t) - \bar{h}$, is then

$$\dot{H} = -H(t) - \frac{2}{\mu}\bar{h}\ H(t-\tau) - \frac{1}{\mu}H^2(t-\tau) \tag{3}$$

Using Eq. 3, it is known that the critical equilibrium $\bar{h}$ of Eq. 2 destabilizes through a (supercritical) Hopf bifurcation scenario as τ crosses from below a critical value $\tau_c(\mu)$ [see (*32*)]. We are then in the presence of a recharge-discharge mechanism rooted into delay effects that causes periodic oscillations.

To design a time-dependent forcing that perturbs the limit cycles emerging through such a Hopf bifurcation, leading eventually to chaotic dynamics according to stretching and folding mechanisms, we first rely on the Hopf normal form of Eq. 3 and the geometric insights recalled in the previous section.

This Hopf normal form is here obtained through Galerkin approximations of Eq. 3 by means of Koornwinder polynomials following Chekroun *et al.* (*32*, *50*), on one hand, and the use of center manifold theory [section 2 in (*51*)], on the other. The result shows that the leading unstable mode's amplitude is approximated, close to $\tau_c(\mu)$, by the following Stuart-Landau (SL) equation

$$\dot{z} = \lambda_1^N z - (\alpha_N + i\beta_N)z|\ z\ |^2 \tag{4}$$

with explicit formulas of the coefficients α_N and β_N given in theorem III.1 in (*32*). The sub- and superscript N reflects the dependence on the dimension N of the Galerkin approximation used to approximate the DDE Eq. 3, i.e., the number of Koornwinder polynomials retained to approximate the DDE solution [see appendix A in (*32*)]. The coefficient λ_1^N denotes the unstable (complex) eigenvalue associated with the linear matrix Γ_N of the Galerkin approximation of Eq. 3 (see note S2). The coefficients α_N and β_N encapsulate the

nonlinear interactions of the corresponding unstable mode $\boldsymbol{e}_1^N$ with the other stable modes [see equations 36 to 39 in (*32*)]. These coefficients control, in turn, the twist of isochrons of the planar limit cycle obtained from Eq. 4, twist that has an intuitive interpretation when Eq. 4 is written in polar coordinates. In these coordinates, (r, ϑ), Eq. 4 becomes the real system

$$\begin{aligned} \dot{r} &= \Re(\lambda_1^N)r - \alpha_N r^3, \\ \dot{\vartheta} &= \Im(\lambda_1^N) - \beta_N r^2 \end{aligned} \tag{5}$$

from which we note the nonlinear dependence of the angular speed $\dot{\vartheta}$ on the radial distance r, whose intensity is controlled by β_N, while $\Im(\lambda_1^N)$ approximates the frequency of the KTF model's limit cycle. As a result, the stronger the β_N (and weaker α_N), the stronger is the radial dependence of the angular speed and thus the shear effects near the limit cycle. This simple observation allows us to understand why the twist number $\gamma = \beta_N/\alpha_N$ provides a good measure of shear effects near the limit cycle (*2*).

For the physical parameter regime corresponding to $\mu = 0.3$ and $\tau = 1$ such as considered in (*31*), the twist number is $\gamma \approx 0.45$ resulting into a moderate twist of the isochrons (see Methods). As a consequence, the shear effects near the limit cycle are too weak to help trigger stretch-and-fold chaos when, e.g., only a random kick in the radial direction is applied to Eq. 4. In contrast, it is shown in Methods a parameter setting for which the twist number is 2.2 corresponding to isochrons that are further bended, becoming more "tangential" to the limit cycle and augmenting thus the shear effects along the limit cycle [see also figure 1 in (*9*)].

Thus, to enhance the shear effects, we apply the following state-dependent perturbation to the SL equation (Eq. 4)

$$F(t,z) = iDf(t)z|\,z\,|^2 + \sigma\dot{W}(t) \tag{6}$$

where $\dot{W}(t)$ is a (real) white noise process, and $f(t)$ is a random kick specified below. The idea is to enhance sporadically the twist number γ to $\gamma + D/\alpha_N$ (thus D must be large enough) while letting the white noise "jiggling" the limit cycle along the real line. Said differently, the term $iDf(t)z|z|^2$ is responsible for enhancing phase diffusion by bending further the isochrons (*52*), i.e., to increase phase-space stretching along the limit cycle as measured in terms of phase difference between two trajectories starting from different isochrons. The term $\sigma\dot{W}(t)$ is aimed at providing the fast fluctuations responsible of the folding through interactions with the nonlinear effects.

The following stochastically perturbed SL equation is then central in the design of the parameters of F to produce noise-driven chaos

$$\dot{z} = \lambda_1^N z - (\alpha_N + i\beta_N)z|\,z\,|^2 + F(t,z) \tag{7}$$

In that respect, the temporal structure $f(t)$ of the state-dependent forcing in Eq. 6 is designed as follows. We take $f(t)$ to be real valued of the form of a square signal, whose activation is randomly distributed in the course of time. More precisely, given a firing rate f_r in (0,1) and duration $\Delta t > 0$, we define the following real-valued jump process as

$$f(t) = \mathbb{1}_{\{\xi_n \le f_r\}}, \quad n\Delta t \le t < (n+1)\Delta t \tag{8}$$

where ξ_n is a uniformly distributed random variable taking values in [0,1] and $\mathbb{1}_{\{\xi \le f_r\}} = 1$ if and only if $0 \le \xi \le f_r$. The choice of the firing rate is important as it must be chosen not "too high" to let express the nonlinear relaxation toward the limit cycle, a key element to produce stretch-and-fold actions. With the right amount of random kicks (controlled by f_r and D) and fast perturbations (controlled by σ), the stochastic forcing F can thus be designed for the stochastic SL equation (Eq. 7) to exhibit shear-induced chaos (see fig. S1).

Recalling that Eq. 4 gives the Hopf normal form of the cloud delay model (Eq. 3), the stochastic perturbation F given by Eq. 6 in Eq. 7 has a useful physical interpretation. As recalled above from (*30*), the lagged effects account for rain production in the formulation of Eq. 3, particularly through the nonlinear term $H^2(t-\tau)$. However, rain is known to be an intermittent phenomenon. On the other hand, the coefficient β_N in the normal form Eq. 4 highly depends on the nonlinear term $H^2(t-\tau)$ [see equations 37 to 39 in (*32*)]. Thus, the term $iDf(t)z|z|^2$, adding to the term $i\beta_N z|z|^2$ in Eq. 4, can be viewed as responsible for enhancing the nonlinear effects caused by rain production in an intermittent way. Within this framework, the white noise term can be interpreted for accounting for turbulent perturbations in a Lagrangian setting (*53*) and F in Eq. 6 for accounting for the missing physics in the KTF model. Note that such a combination of on-off stochastic trigger with white noise has been advocated in the design of conceptual models of precipitation (*54*). For earlier works using stochastic jump processes for parameterizing tropical convection, see (*55*) [see also (*56*–*58*) and references therein].

The question arises then on how to "lift" such a stochastic forcing designed from the low-dimensional, stochastic SL equation (Eq. 7) to (still) produce stretch-and-fold chaos for the DDE (Eq. 3) with infinitely many degrees of freedom. We deal next with this problem of practical importance in view of applications to cloud physics discussed hereafter.

Formulation of the associated stochastic transport problem

As pointed out above, Eq. 4 is a reduced model of Eq. 3 approximating the unstable mode's amplitude near the onset of instability. This model is obtained as the normal form of an N-dimensional Galerkin approximation near the Hopf bifurcation point by application of [theorem III.1 in (*32*)]. Thus, to force Eq. 4 translates into forcing the unstable mode $\boldsymbol{e}_1^N$ of the matrix Γ_N used in the approximation of the linear operator A associated with Eq. 3 (see Eq. 15 below). To assess the effects of such a forcing on the DDE dynamics, one needs then to determine what it means to force this mode in the limit of $N \to \infty$.

To do so, recall that any DDE can be recast into a transport problem for which the solution $u(t,\theta)$ provides, in our case, the historic segment $\{H(t+\theta)\}_{\theta \in [-\tau,0]}$, with $H(t)$ solving Eq. 3 [see, e.g., section II-A in (*32*)]. The Galerkin approximation framework of (*50*) provides rigorous approximations $u_N(t,\theta)$ of $u(t,\theta)$ that are uniform in the time variable, t, and converge in a mean-square sense over the history interval, i.e., for θ in $[-\tau,0]$ [see section 4 and remark in (*50*)]. The DDE solution, $H(t)$, is then obtained as the boundary value $u(t,0)$ by means of numerical schemes exploiting this transport equation reformulation [see, e.g., chapter 3.5 in (*59*) and (*60*)]. Note that DDE solutions obtained this way enjoy better stability properties than by standard step-by-step integration methods applied to the DDE directly (*61*). We refer to (*62*) for a survey about dynamical indicators exploiting the relationships between delay models, and their transport equation formulation

also referred to as the space-time representation of delay models in the physics literature (*63*).

It is within this transport equation formulation that our stochastic parameterizations take place. After mathematical analysis, one can argue that forcing the unstable mode of an N-dimensional Galerkin approximation to Eq. 3 leads, in the limit $N \to \infty$, to the following stochastic transport problem (see Methods and notes S3 and S5)

$$\partial_t u = \partial_\theta u + (F(t, < u, \varphi_1 >)\varphi_1 + \text{c.c.}) \tag{9}$$

subject to the nonlocal and nonlinear boundary condition

$$\partial_\theta u \,|_{\theta=0} = -u(t,0) - \frac{2}{\mu}\bar{h}u(t,-\tau) - \frac{1}{\mu}u^2(t,-\tau) \tag{10}$$

In Eq. 9, φ_1 denotes the unstable mode of the operator A given in Eq. 15 below; it corresponds to the mode that destabilizes through Hopf bifurcation. The stochastic forcing F is given in Eq. 6 but has its argument z therein replaced by the inner product between u and φ_1, namely, $<u, \varphi_1>$ defined in Eq. 16 below. See note S5 for more details.

The effect of this stochastic forcing at the level of the DDE dynamics is then simply obtained by evaluating $u(t,0)$, which reduces to $H(t)$, solving Eq. 3 when F is identically zero. Hereafter, we obtain thus a stochastic version of $H(t)$ [still denoted by $H(t)$] by computing u, solving Eqs. 9 and 10, and storing

$$H(t) = u(t,0) \tag{11}$$

See fig. S9 (C and D) for a numerical illustration of the relationships between $u(t, \theta)$ and $H(t)$.

It is noteworthy that the obtention of stochastic perturbations of deterministic DDE solutions via the stochastic transport formulation (Eqs. 9 and 10) is not purely technical and implies deep differences with forcing stochastically the original DDE by simply adding a stochastic term to the right-hand side (RHS) of Eq. 3. In the latter case, using the transport equation reformulation, the stochastic forcing would appear only in the RHS of the boundary condition (Eq. 10) and not at the transport equation level itself as in Eq. 9. This approach offers more degrees of freedom in the noise design, allowing for taking account of dependence over the past history from $t - \tau$ to t. Furthermore, this stochastic transport framework allows for interpretability of results inspired by the analysis of PDE dynamics such as energy spectra, fluxes through the boundary, and so on (see the "Noise transmission, fluxes, and murmuration cascade" section). Figure 2 provides a schematic of this stochastic transport formulation to generate stochastically perturbed solutions from a given DDE.

Compared to higher-precision schemes (*60*), we observed that numerical solutions to Eqs. 9 and 10 are already computed with high fidelity by using a first-order upwind finite difference scheme following (*59*, *61*) and an Euler-Miruyama scheme for time discretization. For our numerical experiments, unless specified otherwise, we used $\delta\theta = 5 \times 10^{-4}$ and $\delta t = 10^{-4}$. Within this numerical setup, we discuss next the dynamical impact of the stochastic forcing term in Eq. 9 by analyzing the corresponding snapshot attractors.

Noise-driven horseshoes in stochastic transport problems

To compute the snapshot attractors from integration of Eqs. 9 and 10, we proceed in two steps. First, a large number of initial conditions are placed near the limit cycle of the Hopf normal form. Then, we map these initial conditions into functions of the variable θ over $[-\tau,0]$ by using the Koornwinder polynomials (used in the Galerkin approximation) to initiate Eq. 9 accordingly (see Methods). The snapshot attractors obtained by this protocol and shown in Fig. 3 (A and B) reveal an amazing complexity in the reduced state space $[u(t, -\tau), u(t,0)]$ for the forcing parameters as indicated in the caption of that figure. The patterns thus obtained exhibit notable similarities with those displayed by chaotic advection in fluids (*49*, *64*), traditionally associated also with stretching and folding mechanisms as already advanced by Osborne Reynolds [see (*65*) and references therein]. However, we emphasize that in our case, such a fluid-like behavior revealed by the time evolution of snapshot attractors is produced out of a linear advection equation subject to suitable stochastic perturbations (Eq. 9) and to nonlocal and nonlinear boundary conditions (Eq. 10) supporting nonlinear oscillations in the absence of forcing. To the best of the authors' knowledge, our findings constitute among the first numerical evidence that such stochastic transport problems may exhibit, in the appropriate phase space, a behavior highly reminiscent to that of passively advected particles in a turbulent flow (*64*). We mention though (*66*) for a mathematical proof of topological horseshoes arising in deterministic and unforced DDE systems with small delays. Whereas turbulent dynamical systems are generally characterized by both a large dimensional phase space and a large dimension of instabilities, it is thus particularly noticeable that, here, a turbulent behavior is produced still in high dimension but from a system with only one pair of unstable modes associated with the Hopf bifurcation.

Inspired by this fluid analogy, we next examine the mixing in the reduced state space $[u(t, -\tau), u(t,0)]$ by conducting a dye experiment, which consists of marking in red a few points located in a small region of the snapshot attractor (Fig. 3A) and to track its evolution at a later time (Fig. 3B). This numerical experiment reveals the propensity to strong mixing naturally associated with stretching and folding. The dye is stretched following a pattern largely dictated by the unstable manifolds forming striated structures, which spread over the attractor. Compared to its Hopf normal form, the stochastic transport problem (Eqs. 9 and 10) shows snapshot attractors with unstable manifolds presenting occasionally more of such striated structures (compare Fig. 3A with figs. S1, B and C). The additional degrees of freedom appear to amplify the nonlinear shear effects. Movie S1 shows the time evolution of the snapshot attractors obtained from Eqs. 9 and 10 to better appreciate the stretching and folding structures resulting from the interactions between the noise with the nonlinear effects.

Noise-driven murmurations

We consider now the stochastic transport problem (Eqs. 9 and 10) in which the state-dependent forcing term $F(t, \cdot)\varphi_1$ is simply replaced by an additive random kick force $Df(t)\varphi_1$, with $f(t)$ still given in Eq. 8. The idea is to explore the response to a "naive" parameterization that would just use jump processes and not state dependency nor account for turbulent effects (via the σ-term).

With such a forcing, the limit cycle of the SL equation (Eq. 4) does not experience sustained stretch-and-fold deformations anymore and is only substituted by a random periodic orbit (*4*, *67*). However, in this case, we observed that the additional degrees of freedom act as a sort of high-dimensional amplifier of the interactions between the external forcing and the internal

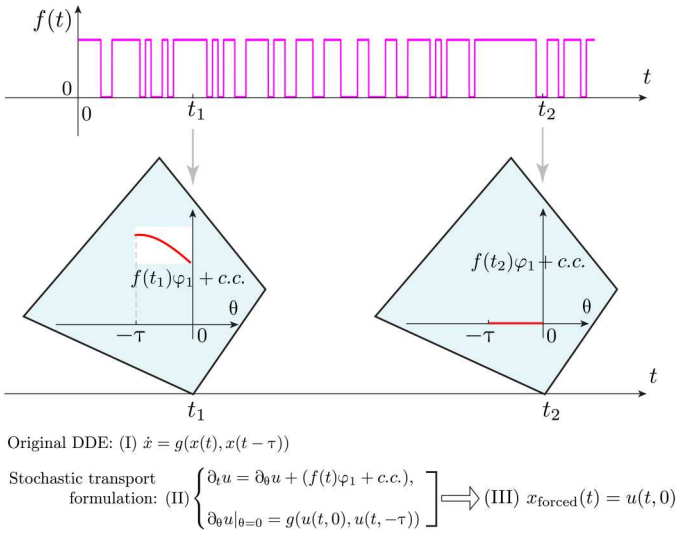

Fig. 2. Stochastic forcing via stochastic transport formulation. In this schematic, the forcing term $F(t, \cdot)\varphi_1$ is an additive random kick force $f(t)\varphi_1$, with $f(t)$ being the jump process given by Eq. 8. It corresponds to the murmuration case discussed in the "Noise-driven murmurations" section. Stochastic perturbations of deterministic DDE solutions are obtained via solving the stochastic transport formulation (II). The forced trajectory is obtained via (III). It is different from forcing the DDE in (I) with $f(t)$ directly, which would consist of forcing the boundary condition $f(t)$ and not forcing the transport equation as in (II).

nonlinear oscillations but in a different way than for the horseshoes case. Eventually, these interactions lead to a new type of noise-driven chaos as revealed by snapshot attractors, which no longer exhibit the stretch-and-fold pattern characteristic of horseshoes (compare Fig. 3, C and D with Fig. 3, A and B). Instead, the points constituting the chaotic PBA evolve in a coherent fashion, reminding that of murmuration, a phenomenon that results when hundreds, sometimes thousands, of starlings fly in swooping, forming intricately coordinated patterns through the sky (*38*) (see Fig. 3, C and D, and movie S2).

Qualitatively, the chaotic dynamics obtained as noise-driven horseshoes, via the state-dependent noise (Eq. 6), or noise-driven murmuration, via additive random kick force, differ from their mixing properties. To visualize this important distinction, a same volume of points colored in red and taken at a same time frame (t = 39) has been propagated by the corresponding stochastic transport problem up to time t = 51, in each case. Figure 3 reports the results of this dye experiment, which shows that the murmuration-like motion is less mixing in the phase space than that associated with horseshoes. On a more quantitative ground, this difference in mixing properties is manifested by a faster decay of correlations in the horseshoes case than in the murmuration case, already visible in the time domain: the time evolution of $H(t)$ presenting faster oscillations in the former case than in the latter (compare red and blue curves in Fig. 4A). See also fig. S7E showing $H(t)$ over a longer time-interval. Last, we would like to emphasize that the "fuzziness" displayed by the snapshot attractors in the murmuration case is presumably indicative of a hyperchaotic behavior with at least two positive Lyapunov exponents (*68*) [see, e.g., figure 1 in (*69*)]. The careful checking of such a hyperchaotic behavior by computation of the Lyapunov exponents is, however, a numerically challenging task for the stochastic transport problems such as Eqs. 9 and 10 due to the high-resolution schemes used in this study.

It is noteworthy that in each case, a noise-driven chaos such as considered here does not correspond to an excitation of a chaotic regime existing nearby in the parameter space as the (deterministic) KTF model is known to exhibit (*31*). The very essence to produce chaotic behaviors here consists of adding the suitable stochastic perturbations to the corresponding transport problems set on the fixed domain [−τ,0], whereas chaos as identified in (*31*) consists of varying the size of this domain, i.e., changing τ. Thus, it is expected that each chaos displays its own spectral signature after estimation of the corresponding (temporal) power spectrum over long simulations corresponding to convergence of the second-order moments (see Fig. 4B). Power spectra are known to relate to structural elements of the dynamical equations (*70*, *71*). While the horseshoes dynamics shows clear distinctions with that of the deterministic chaotic regime, the power spectrum in the murmuration case (Fig. 4B, blue curve) displays some features reminiscent with that of the latter (Fig. 4B, black curve).

Thus, noise-driven chaos produced only under the influence of jump processes (murmuration) is in sharp contrast with noise-driven chaos accounting for state dependency and turbulent effects in their driving noise (horseshoes). The latter exhibits a completely different temporal response than for chaotic behaviors produced by the KTF model alone. Nevertheless, there are still important differences between the murmuration chaos and this deterministic chaos. As explained below, these differences lie in the very level of their generative mechanisms, back to the space-time formulation.

Noise transmission, fluxes, and murmuration cascade

To analyze the mechanisms at the origin of this murmuration chaos compared to those associated with horseshoes or deterministic chaos, we conducted an energy content analysis of high-resolution solutions, $u(t, \theta)$, to Eqs. 9 and 10 (for the corresponding forcing) obtained from long integrations of 2×10^7 iterations. To do so, because the Koornwinder polynomials $K_k^\tau(\theta)$ are naturally ranked from low- to high-frequency wave numbers, k, (see fig. S4A) and form a basis to approximate the solutions of Eqs. 9 and 10 (*50*), we computed the energy content $E(k)$ associated with a wave number k by projecting, for each t, $u(t, \theta)$ onto $K_k^\tau(\theta)$ using the inner product (Eq. 16), followed by time averaging.

We observe that while the energy $E(k)$ decreases monotonically with increasing wave numbers for the unforced chaotic regime, a slower rate of decay of energy of power law type suddenly occurs beyond a critical wave number k_c (~12) in the murmuration case (see Fig. 5, blue curve). The dynamical origin of this notable scaling-law transition is rather subtle. It is tied to the fact that the stochastic perturbation in Eq. 9, in which $F(t, \cdot)\varphi_1$ is replaced by $Df(t)\varphi_1$, is transmitted not only directly within the domain via Eq. 9 but also through the right boundary according to Eq. 10.

To quantify these contributions to the "noise transmission," we computed the rate of change of the flux $\mathfrak{F}_0(t) = \partial_t \partial_\theta u\,|_{\theta=0}$, at the right boundary and within the domain, denoted by $\mathfrak{F}(t, \theta) = \partial_t \partial_\theta u$. By differentiating Eq. 10 with respect to time and using Eq. 9 for computing the corresponding $\partial_t u$-terms, one observes that $\mathfrak{F}_0$ depends on the random kick $f(t)$ in the murmuration case. These kicks occurring irregularly in time cause irregular variations of $\mathfrak{F}_0(t)$ that penetrate within the domain and become

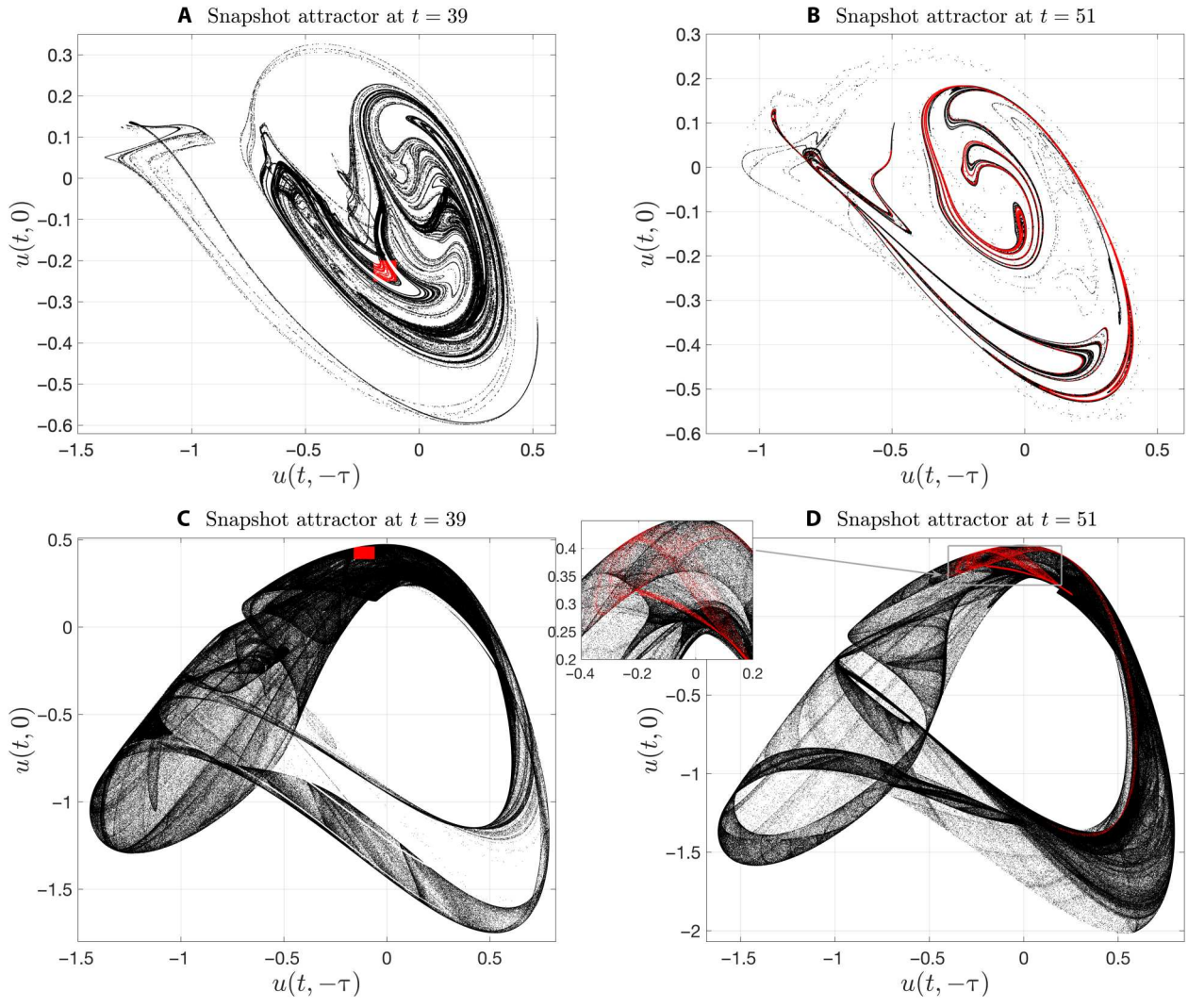

Fig. 3. Snapshot attractors from the stochastic transport problem (): Horseshoes and murmuration cases. Eqs. 9 and 10 (**A**) and (**B**) show the reduced state space, ($u(t, -\tau)$, $u(t,0)$), snapshot attractors, $\mathscr{A}(t)$, at a given time t, as computed by integration of the stochastic transport problem (Eqs. 9 and 10) over 2×10^6 initial data, each driven by the same noise path (see Methods). These panels correspond to the horseshoe case. (**C**) and (**D**) show such snapshot attractors for the murmuration case, which consists of the same protocol, except that the state-dependent noise term $F(t, < u, \varphi_1 >)\varphi_1$ in Eq. 9 is replaced by the additive noise term $Df(t)\varphi_1$ with $f(t)$ given by Eq. 8. In each case, the same volume of points are colored in red at time $t = 39$, whose evolution is shown at time $t = 51$. This dye experiment reveals that the murmuration chaos case is less mixing than for the horseshoe case. The parameter values for the horseshoe case are $D = 60$ and $\sigma = 0.1$, and the parameter value for the murmuration case is $D = 0.3$. In each case, the other parameters are set to $f_r = 0.7$, $\Delta t = 10^{-2}$, $\delta t = 10^{-4}$, and $\delta\theta = 5 \times 10^{-4}$.

manifested spatially (in the θ variable) as small-amplitude high-frequency oscillations on $\mathfrak{F}(t, \theta)$ (t fixed), located near the boundary $\theta = 0$ (see blue curves in fig. S5B).

These oscillations, after integration in time and in θ, become even of smaller amplitudes but are still contained in the solution profile u itself, albeit present only at very weak energy levels. In contradistinction, for the unforced chaotic regime, $\mathfrak{F}_0$ is only driven by the nonlinear dynamics, and $\mathfrak{F}(t, \theta)$ is smooth throughout the domain, including near the boundary $\theta = 0$ (see black curve in fig. S5B). For this deterministic setting, it is thus only (exponential) dissipation that dominates at small scales. For the murmuration case, the small-amplitude oscillations caused within the θ domain by irregular fluxes at the boundary $\theta = 0$ (see inset in fig. S5B) pump up energy into the small scales that manifest into a bending of $E(k)$ toward a slower rate of the form k^{-p} (scale break), as k is increased beyond some k_c.

The transmission of the stochastic perturbations between the domain and the boundary, responsible for the scale break of $E(k)$ in the murmuration case, acts thus as a small-scale stochastic forcing that would be spanned by a few high-wave Koornwinder modes. This observation is consistent with the notable re-emergence of snapshot attractors for the (extremely) small amplitudes associated with scales beyond k_c that are reminiscent with those observed at the large scales [compare Fig. 5 (insets B and C) with Fig. 3, C and D]. At these small scales, the snapshot attractors evoke also in their time evolution the motion of murmuration. We refer to this phenomenon of murmuration across the scales as a murmuration cascade.

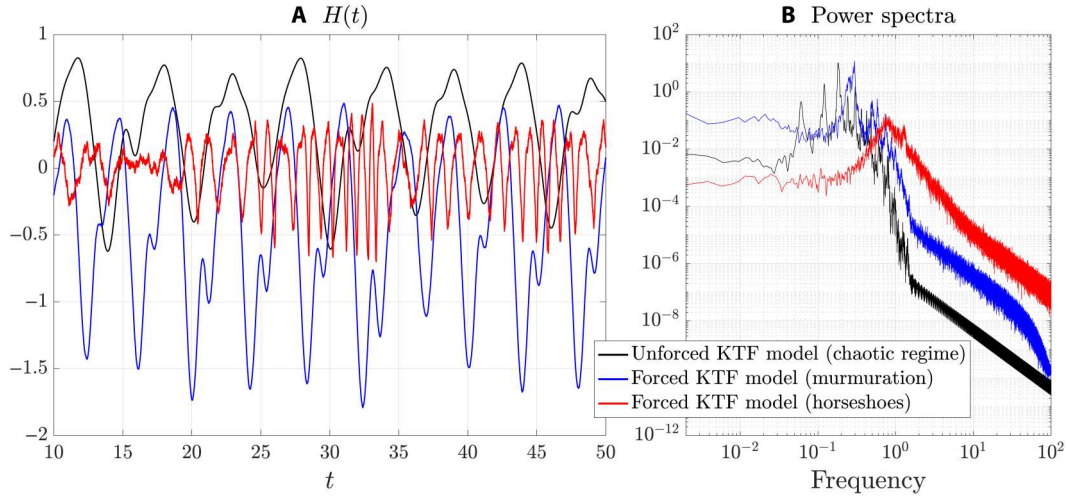

Fig. 4. Comparison of horseshoes and murmuration dynamics. (**A**) Time series of $H(t)$. (**B**) Corresponding power spectra (log-log scale). Shown in each panel is a comparison with a chaotic regime existing nearby in the parameter space (see legend). The horseshoe dynamics is characterized by a dominant oscillation of period $T^* \approx 1$, smaller than the period of the unperturbed KTF model's limit cycle.

We emphasize that such organized dynamics takes place in scales up to seven orders of magnitude smaller compared to the original size of full snapshot attractors shown in Fig. 3 (C and D), expressing almost the signature of self-similarity in these lagged coordinates. This is absolutely remarkable compared to the unforced chaotic regime where, at such scales, any projection of the dynamics is reduced to a "marshmallow-type" shape dominated by dissipation, which also occurs for an intermediate range of scales above k_c in the murmuration case (see Fig. 5, inset A).

For the horseshoes case, recall that the stochastic forcing $F(t, < u, \varphi_1 >)\varphi_1$ in Eq. 9 is also large scale because φ_1 is itself of low wave number in the θ variable (see fig. S4B). The small-scale oscillations exhibited by the profile in θ of $\mathfrak{F}(t, \theta)$ (fig. S5D) are not the fingerprint of the forcing term in the otherwise linear Eq. 9 but rather proceed from the transmission over time of the stochastic perturbations between the domain and the boundary through nonlinear Eq. 10. In this case, this transmission is even more pronounced than in the murmuration case, with a multiplicity of scales of oscillations penetrating deeper into the domain as visible on the θ-profile $\mathfrak{F}(t, \theta)$ shown in fig. S5D. These oscillations are caused by even faster oscillations of $\mathfrak{F}_0(t)$ (due to white noise) at the boundary θ = 0 (compare red and blue curves in fig. S5, C and A, respectively. As a result, the solution's energy in the horseshoes case is distributed according to a power law spanning a wider range of scales than in the murmuration case, explaining the shape of the energy spectrum shown in Fig. 5 (red curve). Here, again, horseshoe-like patterns are visible down the scales on the small-scale projections of the dynamics.

Response dependence to stochastic parameterization

Before comparison with high-end simulations from cloud physics, we report below on a parameter dependence study about the stochastic forcing's parameters and lagged effects. The motivation is to analyze, in terms of variability, the potential diversity of dynamics that the proposed "horseshoe parameterization" provides in view of comparison to other cloud decks observed not only over subtropical oceans but also over continents (*72*). Each of these cellular patterns stems from a distinct dynamical origin (in a physical sense), related to the spatial partitioning of rising and sinking air (*33*, *73*). Thus, we consider below the question of diverse temporal variability produced out of stochastic transport problems such as Eqs. 9 and 10.

Two sets of numerical experiments are conducted in that respect. While keeping fixed the characteristic parameters, D and f_r, of the jump process in Eq. 8, we assess the intensity variation of the turbulent effects encoded by the σ parameter in Eq. 6 upon two periodic nonlinear regimes. One regime, referred to as regime A below, corresponds to the underlying results shown in Fig. 3, i.e., for μ = 0.3 and τ = 1. This regime, which we qualify as mildly nonlinear, is located not far from the Hopf bifurcation with a critical τ value of $\tau_c \approx 0.745$ and with a spectral gap given as $s_g = \Re\lambda_1^N - \Re\lambda_2^N = 1.19$ (see fig. S2, top row). This gap is of size comparable to spectral gaps underlying other parameter regimes for which the center manifold reduction provides efficient low-dimensional approximations of the KTF model's periodic orbits [see section 3.C in (*32*)]. For instance, for τ = 0.8 as in figure 3 in (*32*), $s_g = 1.61$. Recall that the larger the spectral gap, the more auspicious it is for center manifold reduction to operate [see, e.g., equation 2.18 in section 2.1 in (*51*)].

The other regime, referred to as regime B below, corresponds to a strongly nonlinear one (μ = 1.2 and τ = 20) located further away from the onset of Hopf bifurcation with $\tau_c = 6.671$ and with a much smaller spectral gap, $s_g = 3.9 \times 10^{-3}$, than in regime A (see fig. S2, bottom row). For regime B, the limit cycle exhibits more abrupt changes of curvature than in regime A (see magenta curve in Fig. 6A). Physically, by its larger τ value, it corresponds to a situation in which the onset of droplet coalescence to the rain sedimentation is a slower process than for regime A. Without any surprise, for this regime, the center manifold approach fails to provide a reliable low-dimensional approximations (due to small spectral gap) and hence invites us to reconsider the production of noise-driven chaos at the DDE level from a low-dimensional manufacture.

Nevertheless, the stochastic transport formulation (Eqs. 9 and 10), derived from Galerkin approximations in which only the unstable mode is forced stochastically (see note S3), still makes sense to produce for regime B as well, noise-driven chaos as shown below.

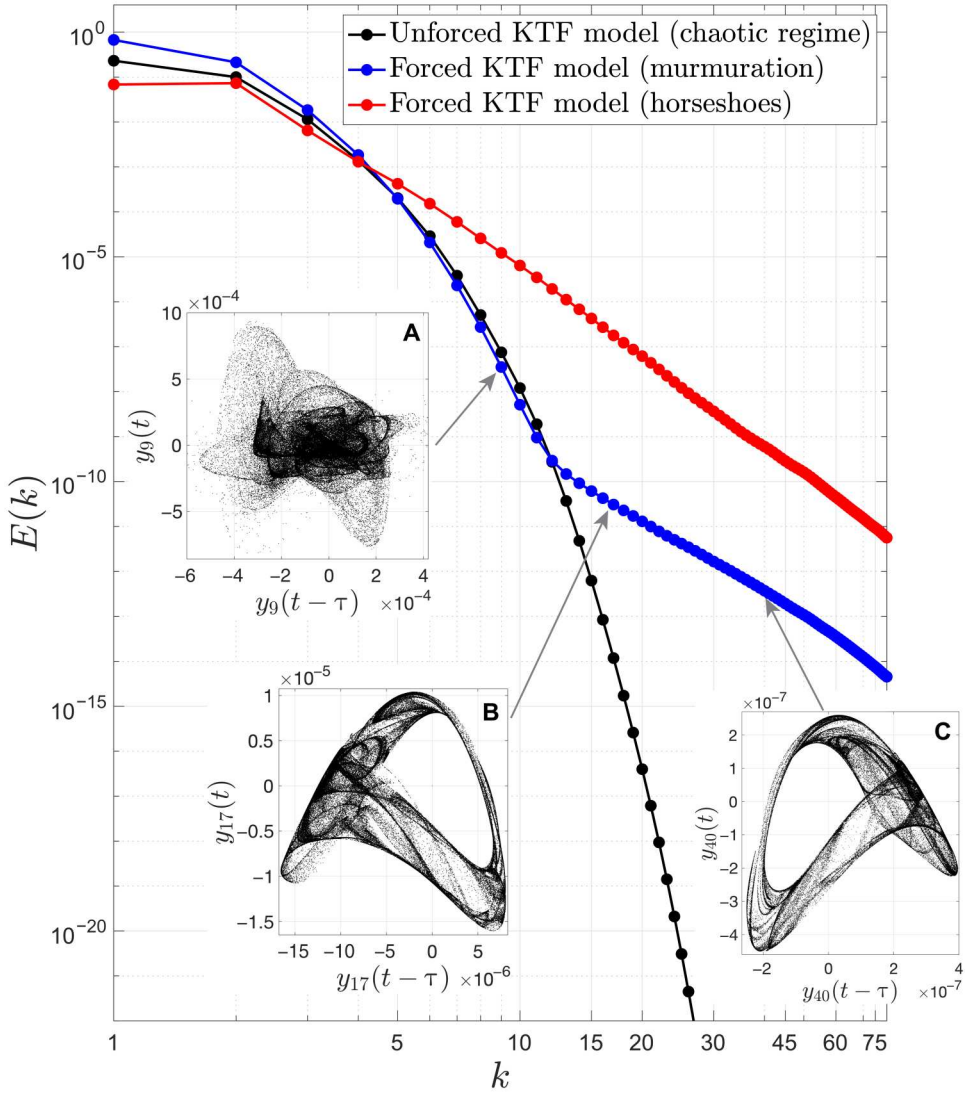

Fig. 5. Energy spectra. These spectra are obtained from discretization of Eqs. 9 and 10 with $\delta\theta = 2^{-12}$ and $\delta t = 10^{-4}$. More precisely, once u is computed for a given type of stochastic forcing, $E(k) = |y_k|^2$, where $y_k(t) = \| K_k^\tau \|^{-1} < u(t,\cdot), K_k^\tau >$, with $\overline{(\cdot)}$ denoting time averaging, and K_k^τ is the (rescaled) Koornwinder polynomial of wave number k [see (*32*) and note S3].

Nevertheless, the insights gained to produce stochastic horseshoes from Eqs. 9 and 10 by further augmenting the isochrons' twist from the reduced SL (Eq. 4),need revision as regime B escapes the domain of validity of center manifold theory. Actually, noise-driven chaos with an even richer temporal variability are reachable when stochastic perturbations of the same form as used in regime A are applied to regime B. We first elaborate on this noise-induced variability and then explain that its origin can still be traced back to low-dimensional mechanisms involving the theory of isochrons.

The diversity in temporal variability can already be visually appreciated by comparing the time series across the regimes [Fig. 6 (C and E) versus fig. S7 (C and E)]. Whereas for both regimes, one departs from randomly kicked periodic oscillations when $\sigma = 0$ and $D \neq 0$ (see Fig. 6A), the emergence of frequency and amplitude modulations displayed by the noise-driven solutions become even more dramatic in regime B compared to regime A as σ is increased (cf. Fig. 6 and fig. S7). The response to stochastic perturbations from Eqs. 9 and 10 in the cases $\sigma = 0.05$ and $\sigma = 0.1$ is marked by "tonic" episodes of high-frequency oscillations (see, e.g., around $t = 160$ in Fig. 6C) that populate a broadspectral peak in the power spectrum (see Fig. 6, D and F and broadband peak marked in red in Fig. 6F).

On the other hand, one observes when $\sigma = 0.05$ and $\sigma = 0.1$, a low-frequency bump pumping out of the power spectrum to the left of this broadband peak (Fig. 6, D and F) manifested in the time domain by episodes of slow and modulated oscillations (Fig. 6E). Note that this low-frequency bump rises above a subharmonic frequency of the (unperturbed) KTF model's period (see the vertical dashed cyan lines across Fig. 6, B, D, and F).

The broad high-frequency peak has an origin that can still be explained by arguments stemming from low-dimensional stochastic dynamics. As mentioned above, normal form theory no longer provides a valid reduction for this regime. On the other hand, the

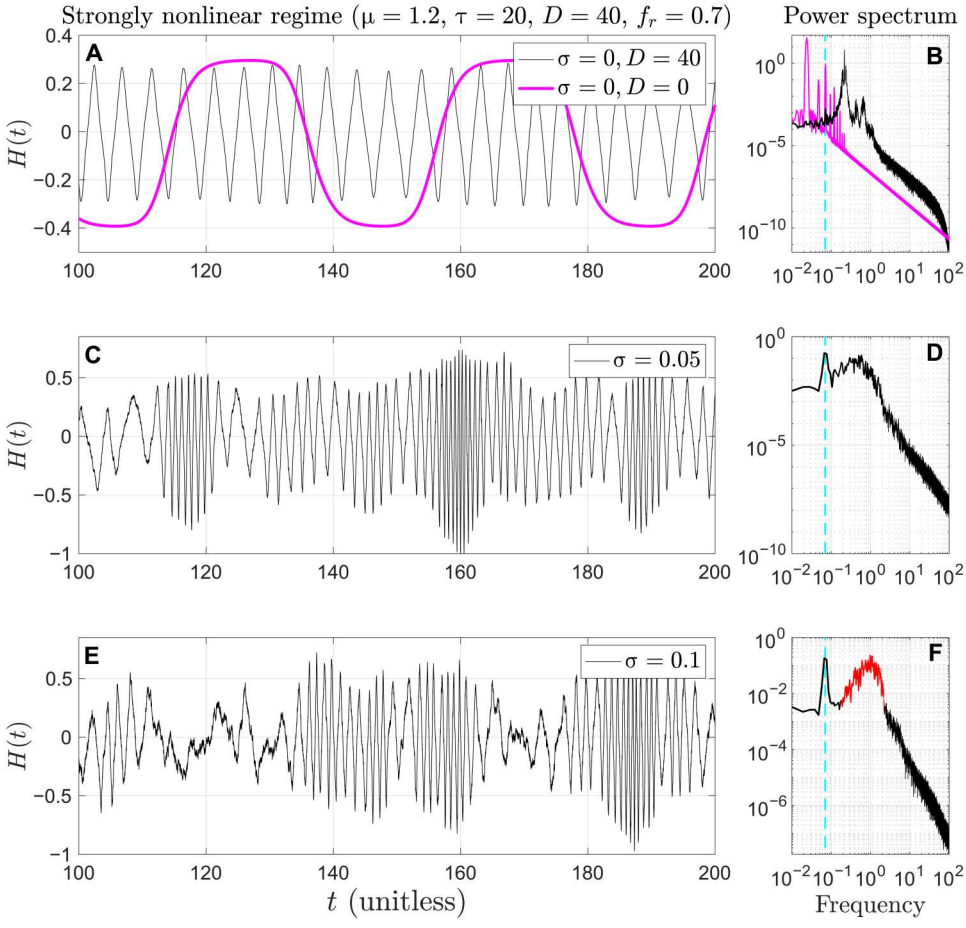

Fig. 6. Parameter dependence of the response: Strongly nonlinear regime away from Hopf bifurcation. (**A**), (**C**), and (**E**) show the response $H(t)$ given by Eq. 11 for different values of σ in the state-dependent noise F (see Eq. 6) with $D = 40$. (**B**), (**D**), and (**F**) show the corresponding power spectra in log-log scale. The magenta curve in (B) corresponds to the power spectrum of the periodic orbit for $D = \sigma = 0$. This periodic trajectory is also shown in magenta in (A). Note the difference in the response to random kicks [black curve in (A)] in terms of the oscillations' near period compared to the original period $T_d \approx 43$ displayed by the unforced DDE's periodic orbit. The response when $\sigma = 0$ and $D = 40$ (A) is oscillating at a faster dominant frequency than T_d^{-1} and, at the same time, much slower than the firing period $\Delta t = 10^{-2}$ of the random kicks. See text for more details.

computation of isochrons is a challenge in dimension higher than three by current mesh-based methods (*74*–*76*), making it difficult to gain insights into the response to perturbations by the computation of the isochrons associated with, e.g., high-dimensional Galerkin approximations (*50*) of the KTF model placed in regime B.

Instead, we adopt a heuristic approach to propose a two-dimensional (2D) reduced system able to approximate with a certain accuracy the 2D projection onto the unstable mode φ_1 of the KTF model's periodic orbit in regime B. This heuristic is described in Methods. It leads, in the (x, y) plane of the corresponding 2D reduced state space, to the following system

$$\begin{aligned} \dot{x} &= Rx + py - c((y + y_*) + b(x - x_*))^3 \\ \dot{y} &= -qx - ry - d(y - y_*)^3 \end{aligned} \tag{12}$$

where R, r, b, c, d, x_*, y_*, p, and q are positive parameters.

The most interesting attribute of Eq. 12 is that it produces a limit cycle with an oblique and elongated shape displaying local changes of curvatures comparable to those of the 2D projection of the KTF model's periodic orbit in regime B (see fig. S9A). The limit cycle from Eq. 12 is shown by the black curve in Fig. 7B (see Methods for the model's parameter values). Unlike in the case of a circular orbit (as for SL Eq. 4), the changes of curvature along the limit cycle imply an inhomogeneous twist of the isochrons. A few isochrons calculated from Eq. 12 and shown in blue in Fig. 7B illustrate this point. This inhomogeneous feature is known to occur for many other 2D systems such as the van der Pol oscillator among others [see figure 10.3 in (*46*) and box C in page 70 in (*43*)]. Such an inhomogeneous twist of the isochrons is also known to affect the response to δ-function perturbations [chapter 10 in (*46*)]. However, little is known regarding the impact of such an inhomogeneous twist of the isochrons on the response to stochastic perturbations. Intuitively, because the angular speed of the unperturbed dynamics is no longer uniform at a fixed radius to the center of gravity of the limit cycle (unlike for Eq. 5), a richer response is expected.

The response of Eq. 12 to stochastic forcing of the form $F(t)$ given by Eq. 6 is thus calculated and shown in Fig. 7A for the x variable in the case of parameter values of F leading to noise-driven chaos. There, we observe, as in Fig. 6E, tonic episodes of high-frequency oscillations punctuated by slower ones. In terms of power

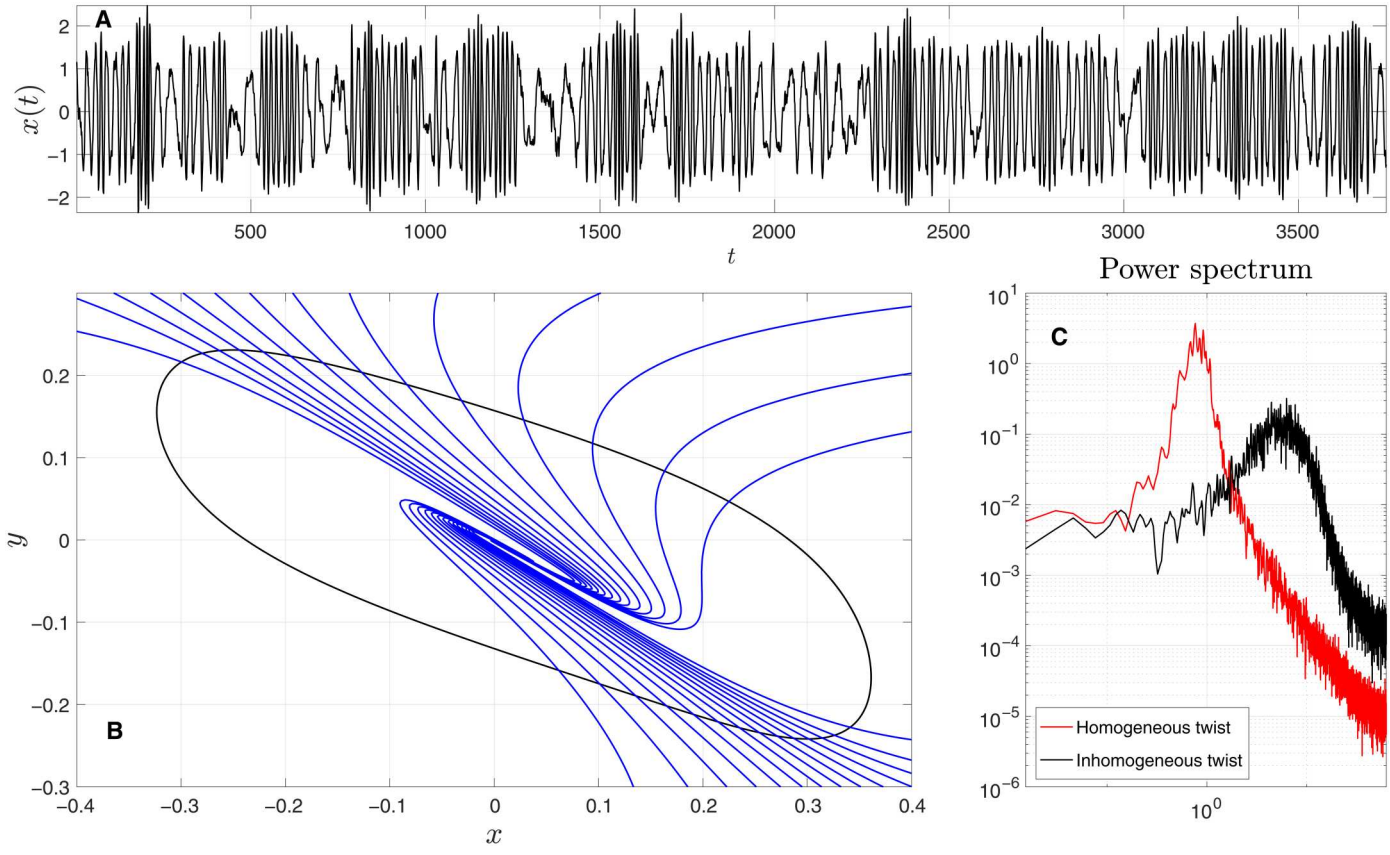

Fig. 7. Broadband response caused by isochrons' inhomogeneous twist. (**A**) The response for the *x* variable to the stochastic perturbation $F(t)$ (given by Eq. 6) applied to the reduced Eq. 12. (**B**) A few isochrons associated with the corresponding limit cycle. (**C**) The power spectrum (in log-log, black) of $x(t)$ shown in (A) and that obtained from SL Eq. 4 when forced by $F(t)$ (red curve). In both cases, the parameters of $F(t)$ are $D = 40$, $f_r = 0.7$, $\Delta t = 10^{-2}$, and $\sigma = 0.1$.

spectrum, these modulations of frequency and amplitude correspond to a broadband peak, which is also skewed toward high frequencies as shown in Fig. 6F for the high-dimensional stochastic transport problem (Eqs. 9 and 10) (compare the black curve in Fig. 7C with the red broadband peak shown in Fig. 6F). In comparison, in the case of an homogeneous twist of the isochrons such as observed for SL Eq. 4 (see Methods), the response to the same stochastic perturbation is not skewed and more narrowband.

It is thus legitimate to attribute the broadband peak of high frequencies observed for Eqs. 9 and 10 to emerge actually from a low-dimensional mechanism, taking its origin into the inhomogeneous twist of the genuine isochrons of the KTF model in the 2D reduced state space associated with the unstable mode φ_1. The low-frequency peak visible in Fig. 6F for Eqs. 9 and 10 is, however, not displayed by the response to the stochastic perturbation $F(t)$ of the reduced equation (Eq. 12). It thus takes a high-dimensional origin presumably rooted into the nonlinear interactions between the noise, $F(t, < u, \varphi_1 >)\varphi_1$, acting along the critical eigendirection, and (some of) the stable eigenmodes.

Last, it is worth noting that the random attractor associated with regime B when $\sigma = 0.1$ displays patterns somewhere in between those shown by the snapshot attractors of Fig. 3 in the horseshoe and murmuration cases, respectively. Such a snapshot attractor for regime B is shown in fig. S9B, and its time evolution is available in movie S3. There, we can distinguish stretch-and-fold features embedded in a "foggier" background than for the snapshot attractors shown in Fig. 3 (A and B) for the mild nonlinear regime, regime A.

Comparison with high-end simulations

Thus, we have just seen that for nonlinear regimes corresponding to conditions in which the onset of droplet coalescence favoring rain is a slow process (regime B) (captured by τ), then the response to stochastic perturbations (missing physics in the KTF model) is of a broader power spectral signature than for regimes with a shorter recharge period before rain sedimentation (regime A).

We illustrate here that the theory presented in the "Noise-driven chaos from delay models" section and insights gained therein enable us to produce stochastically perturbed KTF solutions with a rich frequency content and amplitude modulations that resemble open-cell oscillations as simulated from the high-end WRF model. The benchmark time series is issued from the WRF model simulation (vertical velocity) of an open cell and is obtained by recording the time evolution $w(t)$ of a grid point in Fig. 1B (see the black curve in Fig. 8A). The stochastic perturbations to the KTF model are designed according to the horseshoe's approach, and the model's response is the noise-driven time series $H(t)$ (obtained from Eq. 11), whose an episode is shown in Fig. 8A (red curve). Although $H(t)$ and $w(t)$ are not in the same units, $H(t)$ has been rescaled for a

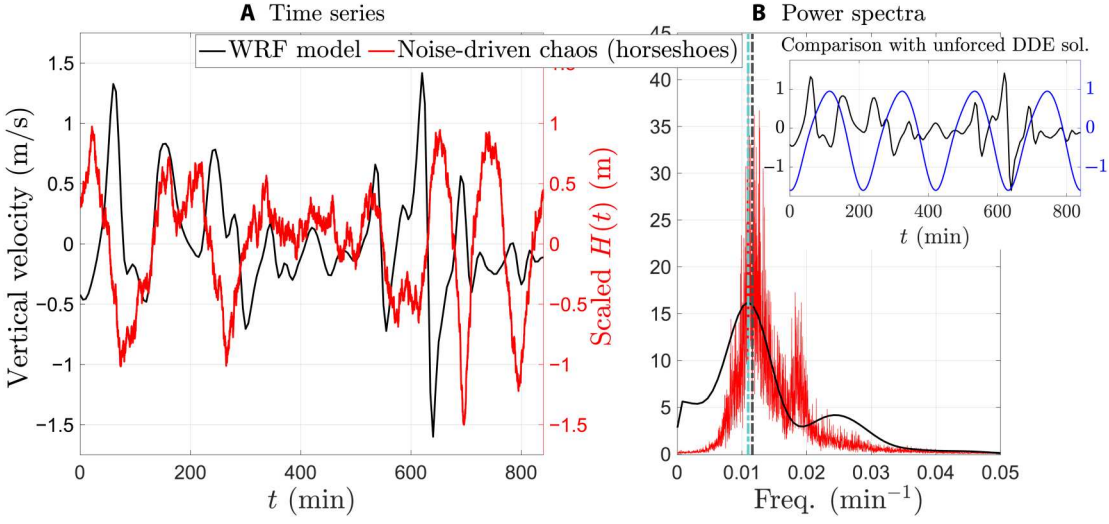

Fig. 8. Noise-driven chaotic time series versus WRF simulation. (**A**) A (rescaled) time series $H(t)$ given by Eq. 11 from the stochastic transport model Eqs. 9 and 10 (red curve) and a time series of the vertical velocity at a spatial location as simulated by the WRF model in the open-cell regime. The corresponding power spectra are shown in (**B**) in linear scale. See text for more details.

better visual comparison, fluctuations in updraft/downdraft being correlated to cloud height.

Regime A turns out to be the most relevant for the comparison exercise. For this regime, the power spectrum of the KTF model's response (red curve in Fig. 8B) shares remarkably similar features compared to the power spectrum of the WRF time series (black curve in Fig. 8B): a low frequency bump and a higher frequency one of smaller energy. This is observed for many such WRF time series of $w(t)$ over the tracked domain shown in Fig. 1B for the open-cell field at hand. There, the dominant period of the most energetic bump is 86.2 min from the noise-driven model Eqs. 9 and 10 matching that of the WRF model. The blue curve shown in the inset of Fig. 8B corresponds to the KTF periodic cycle when the stochastic perturbation in Eqs. 9 and 10 is turned off. Its period is 210.5 min. For comparison, the black curve in the same inset reproduces the black curve shown in Fig. 8A. The stochastic component is thus able to rectify significantly delay-induced periodic oscillations toward realistic ones. To "optimize" these results, note that the time in the KTF model has been rescaled as $t = st$, where $s = f^*_{\mathrm{KTF}}/f^*_{\mathrm{WRF}}$, in which f^*_{KTF} denotes the frequency of the dominant peak in the KTF model's response (before rescaling), while f^*_{WRF} denotes that of the WRF time series. With this rescaled time, the value of the rescaled τ is 66 min, while μ = 19.8. The noise parameter values are given in Methods.

It is noteworthy that the stochastically perturbed normal form (Eq. 7) of the KTF model [with F given by Eq. 6] allows for approximating the frequency f^*_{KTF} of the dominant peak in the KTF model's response to stochastic perturbations.

Without noise, the fundamental frequency f_c to Eq. 7 is obtained thanks to Eq. 5 as $f_c = \Im(\lambda_1^N) - \Re(\lambda_1^N)\beta_N/\alpha_N$, dropping the $1/(2\pi)$ factor. When noise is turned on, the term $\eta(t) = Df(t)r^2$ (see Eq. 8) is added to the RHS of the θ equation of Eq. 5, which perturbs therefore this fundamental frequency. By simply making the approximation $\eta(t) \approx Df_r\bar{r}^2$, with $\bar{r}$ denoting the mean value of the r fluctuations, the dominant frequency of $z(t)$ solving Eq. 7 is then approximated by

$$f^\star = \frac{f_c + Df_r\bar{r}^2}{2\pi} \tag{13}$$

It turns out that $f^\star$ provides a good approximation of f^*_{KTF} with $f^\star$ corresponding to a dominant period of 91 min (see the two dashed vertical lines in Fig. 8B with black for f^*_{KTF} and cyan for $f^\star$).

However, this normal form approximation is unable to explain the second bump in the power spectrum of the KTF model's response, because the latter does not correspond to a "subharmonic" of f^*_{KTF}. Neither it corresponds to a "fingerprint" frequency inherited from the forcing $f(t)$, the latter presenting a flat spectrum over a low-frequency band containing the frequency peak of this second bump (see inset figure in fig. S8).

Recall that the Koornwinder polynomials allow for decomposing the solution $u(t, \theta)$ to Eqs. 9 and 10 according to

$$u(t,\theta) = \sum_{k=0}^{\infty} y_k(t) K_k^\tau(\theta) \tag{14}$$

where K_k^τ denotes the rescaled (and normalized) Koornwinder polynomials (*50*), and $y_k(t)$ denotes the corresponding Koornwinder coefficients. By analyzing the power spectra of these coefficients, one observes that the second bump is not only present in them but dominates their time variability, starting from the third (i.e., k = 3) Koornwinder coefficient (see the bump marked by a vertical dashed line in each panel of fig. S8). This observation together with the decomposition formula (Eq. 14) shows that the time fluctuations carried by the high wave number modes participate to the second bump exhibited by the (temporal) power spectrum displayed in Fig. 8B.

DISCUSSION

Thus, different types of noise-driven chaos—produced from either low- or high-dimensional interactions between the noise and

nonlinear terms—have been identified and implemented for the KTF model. From a cloud physics perspective, this work brings new perspectives on the impact of fast fluctuating processes (microphysics/turbulence) onto the cloud large-scale motion, modeled as delay-induced oscillations, depending on the way these processes are parameterized. We have shown that the latter may induce on the large-scale dynamics completely different cloud dynamics' responses, responsible of irregular oscillations with their own spectral properties.

Notably, when the stochastic forcing, F, accounts for intermittent rain production and Lagrangian turbulent effects (missing physics in the original KTF model) as in Eq. 6, it enables us to produce stochastically perturbed KTF solutions with a rich temporal variability that resembles open-cell oscillations as simulated by the high-end models of cloud physics (see Fig. 8).

The low-dimensional mechanism through which the regular oscillations (limit cycles) are stretched and folded by F (with suitable parameters) until emergence of stochastic strange attractors (stochastic horseshoe-like structures) mirroring the motion of passive tracers in a turbulent flow is not limited to the KTF model. This phenomenon is generic as we have shown that the very fabric of such a noise-driven chaos is rooted into the center manifold reduction of any time delay system exhibiting a Hopf bifurcation [theorem III.1 in (*32*)], on one hand, and the theory of shear-induced chaos (*2*), on the other. Figure 9 shows these generic mechanisms at work to produce systematically stochastic horseshoe-like structures from stochastic perturbations of delay-induced periodic oscillations as long as the DDE model is placed not "too far" after the onset of a (supercritical) Hopf bifurcation such that center manifold reduction techniques apply.

In contradistinction, noise-driven horseshoes can no longer be predicted by center manifold and normal form theory for strongly nonlinear regimes exhibiting limit cycles, which are distorted in the absence of noise. Still, the theory of isochrons and the stochastic transport formulation provide a flexible framework to understand and produce noise-driven chaos—with an even richer temporal variability—from stochastic perturbations of such highly nonlinear DDE limit cycles as documented in the "Response dependence to stochastic parameterization" section. With the proper reduced equation to approximate the unperturbed limit cycle in the unstable space, we have shown that the reduced equation's isochrons are still key elements in the design and production of noise-driven chaos for the full model.

The open-cell field analyzed in this study (see Fig. 1) revealed that stochastic perturbations to the KTF dynamics such as obtained via the stochastic transport formulation (Eqs. 9 and 10) provides good approximations of the time variability of the open cells, in the case of a mild nonlinear regime (regime A), corresponding to relatively short recharge period before rain sedimentation (see the "Comparison with high-end simulations" section). Obviously, open cells in stronger nonlinear regimes with longer time to rain sedimentation can also be found in nature depending, e.g., on the concentration of aerosols (higher μ values as in regime B), and this is where the ideas discussed in the "Response dependence to stochastic parameterization" section could show their physical relevance. We are aiming to explore the occurrence of such regimes from observations in the future.

It is also worthwhile noting that noise-driven murmurations [$F = Df(t)$ with $f(t)$ given by Eq. 8] cannot be predicted by normal form theory. The reason does not lie though in the nonproximity to the onset of Hopf bifurcation. Noise-driven murmurations have been shown to occur for randomly kicked DDE's limit cycles located near this onset, albeit such murmurations are not emerging from perturbations of the normal form alone. The loss of predictability of murmurations from the normal form lies elsewhere. Noise-driven murmurations are the result of a high-dimensional manufacture in which the noise acting along the critical eigendirection is transmitted through the nonlinear terms to stable modes located deeper into the linear spectrum.

With its re-emergence of organized structures at very small scales (see Fig. 5, B and C, insets), noise-driven murmurations exhibit a somewhat loftier root than its horseshoes counterpart, which constitutes to the authors' opinion, a mesmerizing finding of this work that requires even further substantiation for other fields of applications. It seems that noise-driven murmurations are not just a distinctive quality of the KTF model but could be produced for other DDE models such as arising in, e.g., population dynamics (*15*).

This observation opens up new horizons in terms of characterization of the (genuine) phenomenon of murmuration (*38*). It suggests that such phenomena made of synchronous and asynchronous dynamics [chimera states (*77*)] may result from stochastic perturbations of delay-induced periodic oscillations.

More generally, the stochastic and nonlinear mechanisms brought to light in this study to obtain in a systematic fashion, enriched oscillatory patterns from periodic oscillations caused by delay effects, are expected to nurture new ideas for the modeling of many oscillatory phenomena. For instance, the incorporation of stochastic effects to physiological delay effects present in standard cardiac electrophysiology models (*78*, *79*) could potentially contribute to improve the understanding of episodes of ventricular fibrillations (in terms of their dynamics) in view of their control or prevention.

Going beyond the realm of delay models, our approach is also expected to be applicable to PDEs that admit regular oscillations through Hopf bifurcations. Such models supporting Hopf bifurcations spread a wide array of scientific and engineering applications (*80*, *81*). The stochastic perturbations mechanisms and details about their numerical implementation identified here have a great potential to enable the practitioner to reach realistic regimes from computationally friendly ones by stochastically rectifying periodic oscillations into enriched oscillatory patterns in terms of their temporal variability. In that respect, the role of stochastic oscillators in parameterization (*82*, *83*) has already demonstrated certain promises that comfort such ideas.

METHODS

The WRF model

In our WRF simulations using the Advanced Research WRF core (*41*), the prognostic variables (including vertical velocity) are obtained by using the National Centers for Environmental Prediction FNL (Final) Operational Global Analysis data on 1° × 1° grids prepared operationally every 6 hours for the day of interest (here 18 January 2020). The model topography and other static surface fields are initialized with high-resolution global databases. A snapshot of the vertical velocity field just below the cloud base (~750 m) as modeled by the WRF model is shown in fig. S10. To obtain these

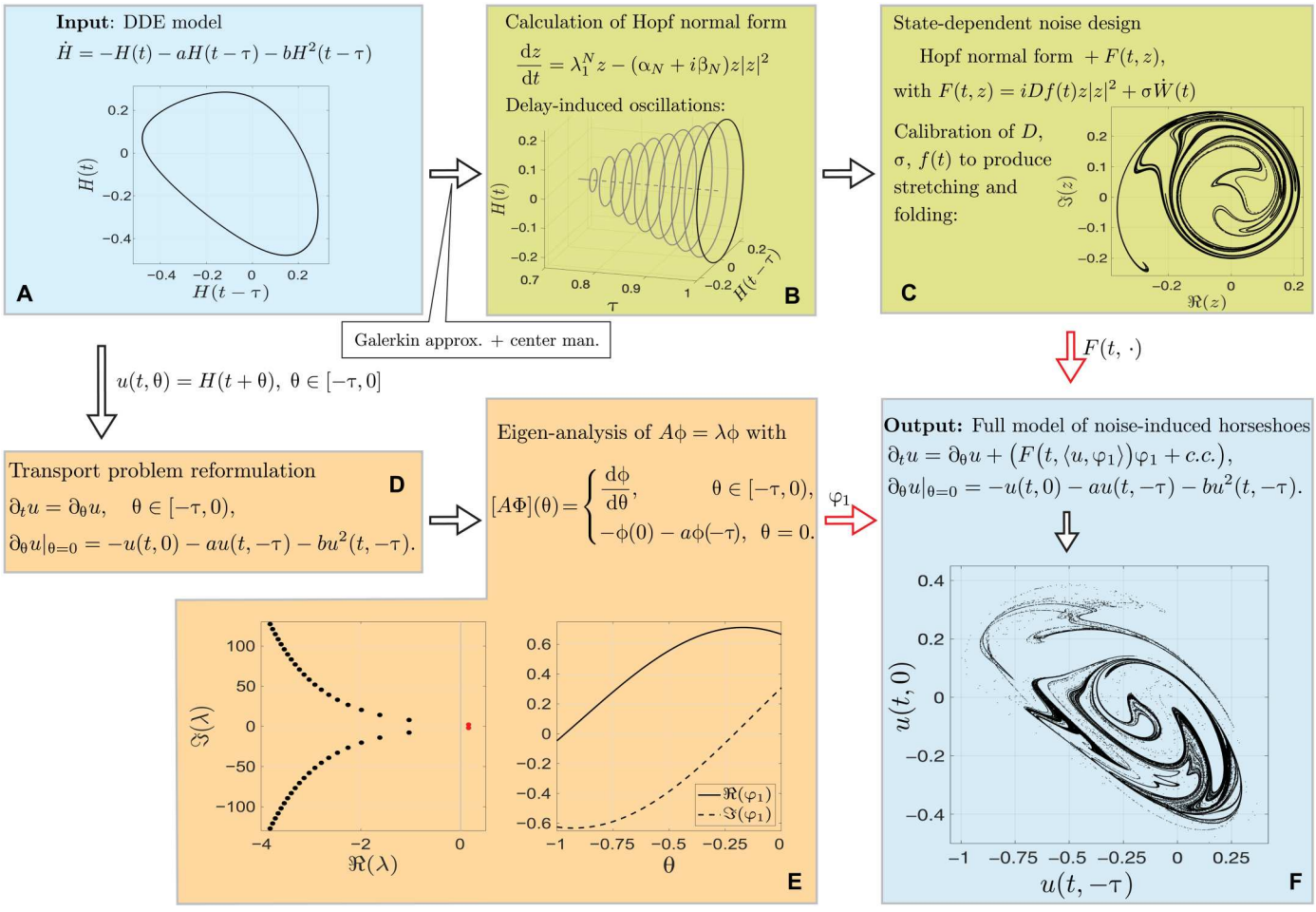

Fig. 9. Generic mechanisms to produce stochastic horseshoe-like structures from a DDE experiencing a Hopf bifurcation: Schematic chart. Here, the main steps to produce stochastic horseshoe-like structures from the KTF model are summarized. The latter serves just as an illustration and can be replaced by any other DDE model experiencing a delay-induced (supercritical) Hopf bifurcation. First, the Hopf normal form's coefficients in Eq. 4 of the corresponding DDE model are computed following, e.g., theorem III.1 in (*32*) (**A** and **B**). Then, its stochastic version (Eq. 7) is used to design the parameters of the state-dependent noise $F(t, z)$ given in Eq. 6 to obtain noise-driven chaos as shown in (**C**). In parallel, in (**D**) and (**E**), the unstable mode φ_1 of the linear operator A is computed; here, φ_1 associated with the unstable pair [red dots in (E), left inset] is shown in (E) (right inset) for the KTF model. By using $F(t, \cdot)$ and φ_1 as obtained in (C) and (E), respectively, to force what would be the analog of Eqs. 9 and 10 for another DDE model (**F**), one would get the production of stochastic strange PBAs exhibiting horseshoe-like structures. This latter statement is valid as long as the DDE model is placed not too far after the onset of a (supercritical) Hopf bifurcation such that center manifold reduction techniques apply. For situations violating these conditions, one can still apply the stochastic parameterization approach shown here to predict (and characterize) noise-driven chaos for the stochastic transport problem, albeit from reduced equations different from the SL (Eq. 4) (see the "Response dependence to stochastic parameterization" section).

results, our simulations are run with two nested domains (no feedback from the inner nests) and 95 vertical layers between the surface and 50 hPa. Our analyses focus on the outputs of the inner domain only, with a horizontal resolution of 3 km, a time resolution of 5 min, and a gradually increased vertical resolution that ranges from 5 to 500 m. Our simulations use a Thompson aerosol-aware scheme for the microphysics (*84*) and the Rapid Radiative Transfer Model (RRTM) for general circulation models (GCMs) for longwave and shortwave radiation. The subgrid-scale turbulence is parameterized by using a Yonsei University scheme, which consists of a nonlocal K scheme with explicit entrainment layer and parabolic K-profile in the unstable mixed layer (*85*). A revised fifth-generation Pennsylvania State University–National Center for Atmospheric Research Mesoscale Model with Monin-Obukhov scheme is used for the surface layer (*86*). Last, the advection scheme uses the positive-definite advection option for the ARW solver, which is set by default in the WRF model and is recommended for real-data simulations as in this stud [see (*41*)].

Isochrons of the Hopf normal form (Eq. 4)

To help provide an intuitive understanding about the isochrons, we show in Fig. 10 the geometry formed by the isochrons for the Hopf normal form (Eq. 4), as computed following the chapter 10 in (*46*). We also show a case for which the twist number is increased to exemplify the effect on the bending of isochrons. See the caption of Fig. 10.

Forcing the unstable mode in the limit $N \to \infty$

It is by adopting the transport equation reformulation of a DDE and its Koornwinder-Galerkin approximation (*32*) that one can make

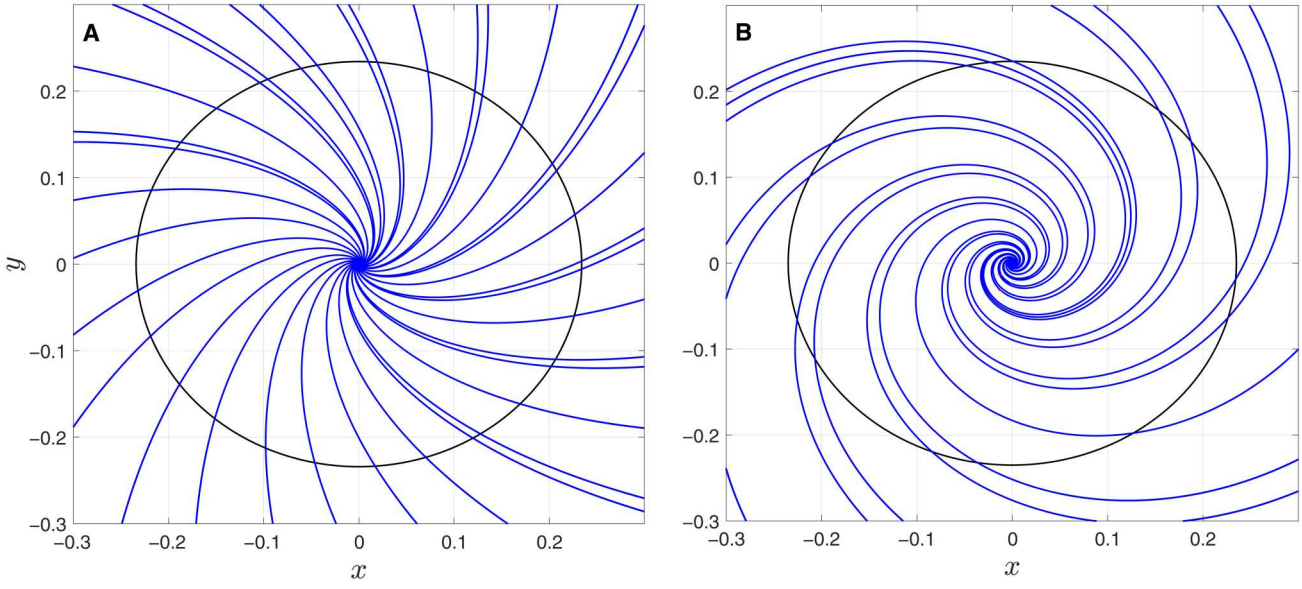

Fig. 10. Isochrons. The isochrons' twist measures the phase-space stretching near the limit cycle. (**A**) A few isochrons, shown as blue curves, are computed for the SL (Eq. 4) with $\lambda_1^N = 0.158 + 2.079i$, $\alpha_N = 2.893$, and $\beta_N = 1.307$. The limit cycle is shown in black. These coefficient values correspond to those of Eq. 2 for $\mu = 0.3$ and $\tau = 1$, i.e., for a regime near the instability onset. (**B**) Same when β_N is replaced by $\beta_N + D$ with $D = 5$ corresponding to a twist number $\gamma \approx 2.2$. One observes as D is increased that the new isochrons are further bended compared to the $D = 0$ case shown in (A), augmenting the shear effects along the limit cycle.

precise what it means to force the unstable mode in a Galerkin approximation of Eq. 3 when taking the limit. To do so, note that, using the Koornwinder polynomials, the (Galerkin) unstable mode $\boldsymbol{e}_1^N$ has a natural representation in the θ variable given by $\varphi_1^N(\theta) = \sum_{j=1}^N e_{1,j}^N K_j^\tau(\theta)$ for θ in $[-\tau,0]$, where the K_j^τ denote the (rescaled) Koornwinder polynomials [see A.10 in (*32*) and note S3]. As N tends to infinity, such eigenelements converge to those of the following linear operator A acting on $\Phi = (\phi, \phi(0))$ (with ϕ in a suitable function space over $[-\tau,0]$) (*50*).

$$[A\Phi](\theta) = \begin{cases} \dfrac{d\phi}{d\theta}, & \theta \in [-\tau, 0), \\ -\phi(0) - \dfrac{2}{\mu}\bar{h}\phi(-\tau), & \theta = 0 \end{cases} \tag{15}$$

More precisely, denoting by (λ_1, φ_1) [respectively $(\lambda_1^N, \varphi_1^N)$], the leading eigenpair of A (respectively the Nth Galerkin truncation of A), we have, as $N \to \infty$, that $|\lambda_1^N - \lambda_1|$ and $\|\varphi_1^N - \varphi_1\|$ converge to 0 (see figs. S3 and S4). Here, $\|\cdot\|$ denotes the norm associated with the inner product of the Hilbert space $L^2([-\tau,0);\mathbb{R}) \times \mathbb{R}$, namely, the inner product defined for any $\Phi = (\phi, x)$ and $\Psi = (\psi, y)$ by

$$\langle \Phi, \Psi \rangle = \frac{1}{\tau}\int_{-\tau}^{0} \phi(\theta)\psi(\theta)\, d\theta + xy \tag{16}$$

where x and y denote point values at $\theta = 0$. See notes S5 and S3 for the derivation of the stochastic transport problems in the horseshoe case and the murmuration case, respectively.

Snapshot attractors computation: Initial data generation

We describe next how the initial data used for the computation of the stochastic transport problem snapshot attractors are generated. Recall that a snapshot attractor is given by an ensemble of trajectories that start from a set B of initial states in the phase space and that are driven by a common noise path once a finite amount of time s has elapsed (*4*, *5*). Thus, a snapshot attractor provides the instantaneous distribution at the current time t of many "particles" emanating from B at time t-s and driven by a same forcing. When s is sent to infinity and B is varied in an admissible class of subsets of the state space, X, one obtains the PBA, $\mathscr{A}(t)$, of the system. The latter thus describes the system's states in X that are reached at a time t when the system is initiated from an asymptotic past, $s' = t - s \to -\infty$, and the initial states are varied within, e.g., a collection of bounded sets of X. One of the main teachings of the PBA approach is that even under the presence noise, if an ensemble of trajectories is examined, each driven by the same noise path, then, e.g., the fractal structure of an underlying chaotic dynamics can be faithfully revealed (*4*). As discussed above, the way the noise enters the model's equations plays a determining role in that respect. Key also is the generation of a sufficiently diverse population of initial data to reveal the possible PBA's complex structures.

This is a challenge for the stochastic transport problems considered here. Recall that these problems are high-dimensional because, after discretization, they lead to solving stochastic differential equations with up to 4096 degrees of freedom. Thus, the choice of initial data must be operated with care to sample regions that are dynamically meaningful within such a high-dimensional state space [see also (*25*)]. The general idea we pursue here exploits the perturbation setting of our problem. In that respect, the population of initial data is chosen near the unperturbed KTF limit cycle. To do so, we exploit low-dimensional approximations as provided by the Galerkin-Koornwinder (GK) framework (*50*).

More precisely, we first simulate an N-dimensional GK approximation of the unforced KTF model to resolve the limit cycle. For this purpose, we have used a semi-implicit Euler scheme to solve the GK system with a time step $\delta s = 1/2^{10}$ for the simulation of a GK system with $N = 20$, which already allows for an approximation of the KTF model's limit cycle to a very high precision.

After the removal of the transient dynamics to allow the dynamics for settling down on the limit cycle, we then extract the solution segment over one period (associated with the sampling rate δs) that we denote by $\{\boldsymbol{y}^j : j = 1, \cdots, p\}$. This solution segment is then projected onto the eigenvectors $\{\boldsymbol{e}_k^N : k = 1, \ldots, N\}$ of the matrix $\Gamma_N(\tau)$ involved in the GK approximation of Eq. 3 (see note S2) to get $\{z_k^j : j = 1, \ldots, p, k = 1, \ldots, N\}$. Here, on average, the first two modes account for more than 99% of the limit cycle's energy for regime A and about 75% for regime B. Recall that the second mode is just the complex conjugate of the first mode. In other words, the N-dimensional vectors $(z_k^j)_{k=1}^N$ are, on average (over j), quasi-bidimensional, i.e., close or even very close (regime A) to the 2D plane spanned by z_1^j and $z_2^j = \overline{z}_1^j$.

It is by relying on such high-energy approximations provided by the pair of leading modes that we design the random samples generating the desired initial data. To do so, to each data point z_1^j (and its complex conjugate), we draw q samples of a uniformly distributed random variable ξ, for which $\Re(\xi)$ is uniformly distributed in $[\Re(z_1^j) - \delta, \Re(z_1^j) + \delta]$ and $\Im(\xi)$ is uniformly distributed in $[\Im(z_1^j) - \delta, \Im(z_1^j) + \delta]$, with $\delta = 0.01$ for regimes A and B.

The resulting sample points are denoted by $z_1^{j,\ell}$ for $j = 1, ..., p$ and $\ell = 1, ..., q$, where j marks out the "location" on the limit cycle, and ℓ labels the sample points at this jth site. Then, by introducing

$$\boldsymbol{y}^{j,\ell} = (z_1^{j,\ell}\boldsymbol{e}_1^N + \text{c.c.}) + \sum_{k=3}^{N} z_k^j \boldsymbol{e}_k^N \tag{17}$$

the initial data for Eqs. 9 and 10 are taken to be $\phi_{j,\ell} = \sum_{n=1}^{N} y_n^{j,\ell} K_n^{\tau}$, where $y_n^{j,\ell}$ denotes the nth component of $\boldsymbol{y}^{j,\ell}$. In the numerical results shown in Fig. 3, we have $p = 3214$ and $q = 600$, leading to about 2×10^6 initial data, $\phi_{j,\ell}$, to compute the corresponding snapshot attractors shown in Fig. 3 and in movies S1 and S2. Movie S3 associated with regime B is produced by using 2.5×10^5 initial data due to the longer spin-up time before reaching the random attractor.

The reduced Eq. 12 for regime B

The study of the linear part of Eq. 12 reveals that when $2pq > (r + R)^2$, linear instability is produced with linear growth $(R - r)/2$ and oscillatory frequency $\omega = \sqrt{pq - (r+R)^2/4}$. When $R = r$, the growth rate is zero, and thus, the linear system exhibits a perfect harmonic oscillatory solution with frequency ω_c whose analytic expression is given by $x(t) = x_0 \cos(\omega_c t) + (rx_0 + py_0) \sin(\omega_c t)/\omega_c$ and $y(t) = -qx(t - t_c)/\sqrt{\omega_c^2 + r^2}$ with $t_c = \arctan(\omega_c/r)/\omega_c$. This latter relation between $y(t)$ and $x(t)$ shows that this harmonic oscillation gives rise to an oval-shaped closed orbit in the (x, y) plane with a "major" direction from the top left to the bottom right quadrant.

These orbit's shape and location in the (x, y) plane are in agreement with that of the 2D projection onto the unstable mode φ_1 of the KTF model's periodic orbit in regime B (see fig. S9A). The cubic nonlinear terms in Eq. 12 saturate the growth rate to a self-excited oscillation of finite amplitude (limit cycle) whose orbit shares a similar oblique direction in the (x, y) plane as for the harmonic oscillation, as long as d and c are sufficiently small. When the two closed orbits intercept, i.e., the limit cycle from Eq. 12 and the 2D projection of the DDE's periodic orbit, the parameter values in Eq. 12 are then chosen to minimize the error, which consists of the area formed by the union of their respective enclosed domains to which is subtracted that of their intersection. With the following choice of parameters, $R = 0.599$, $r = 0.25$, $p = 0.75$, $q = 0.267$, $b = 2.132$, $c = 0.45$, and $d = 0.5$, while $x_* = 0.065$ and $y_* = 0.12$, one reaches a nearly optimal solution corresponding to a relative error of about 7%.

The noise parameters for Fig. 8

In the rescaled time used to obtain the results of Fig. 8, the noise parameters values are $D = 0.909$, $D = 0.909$, $\sigma = 0.1/\sqrt{66}$, and $\Delta t = 0.66$, while $f_r = 0.7$.

Supplementary Materials

This PDF file includes:

Notes S1 to S5
Figs. S1 to S10
References

Other Supplementary Material for this manuscript includes the following:

Movies S1 to S3

REFERENCES AND NOTES

1. B. Van der Pol, J. Van Der Mark, Frequency demultiplication. *Nature* **120**, 363–364 (1927).
2. L.-S. Young, Generalizations of SRB measures to nonautonomous, random, and infinite dimensional systems. *J. Stat. Phys.* **166**, 494–515 (2017).
3. J. Guckenheimer, M. Wechselberger, L.-S. Young, Chaotic attractors of relaxation oscillators. *Nonlinearity* **19**, 701–720 (2006).
4. M. D. Chekroun, E. Simonnet, M. Ghil, Stochastic climate dynamics: Random attractors and time-dependent invariant measures. *Physica D* **240**, 1685–1700 (2011).
5. T. Bódai, G. Károlyi, T. Tél, A chaotically driven model climate: Extreme events and snapshot attractors. *Nonl. Proc. Geophys.* **18**, 573–580 (2011).
6. Q. Wang, L.-S. Young, Strange attractors in periodically-kicked limit cycles and Hopf bifurcations. *Commun. Math. Phys.* **240**, 509–529 (2003).
7. Q. Wang, L.-S. Young, Strange attractors with one direction of instability. *Commun. Math. Phys.* **218**, 1–97 (2001).
8. Q. Wang, L.-S. Young, Toward a theory of rank one attractors. *Ann. Math.* **167**, 349–480 (2008).
9. S. Wieczorek, Stochastic bifurcation in noise-driven lasers and Hopf oscillators. *Phys. Rev. E* **79**, 036209 (2009).
10. K. C. A. Wedgwood, K. K. Lin, R. Thul, S. Coombes, Phase-amplitude descriptions of neural oscillator models. *J. Math. Neurosci.* **3**, 2 (2013).
11. P. Ashwin, S. Coombes, R. Nicks, Mathematical frameworks for oscillatory network dynamics in neuroscience. *J. Math. Neurosci.* **6**, 2 (2016).
12. K. K. Lin, L.-S. Young, Shear-induced chaos. *Nonlinearity* **21**, 899 (2008).
13. K. Lu, Q. Wang, L.-S. Young. *Strange Attractors for Periodically Forced Parabolic Equations*, volume 224 of *Memoirs of the American Mathematical Society* (American Mathematical Society, Providence, RI, 2013).
14. G. A. Bocharov, F. A. Rihan, Numerical modelling in biosciences using delay differential equations. *J. Comp. Appl. Math.* **125**, 183–199 (2000).
15. J. D. Murray, *Mathematical Biology: I. An Introduction* (Springer, 2002).
16. K. Bansal, J. O. Garcia, S. H. Tompson, T. Verstynen, J. M. Vettel, S. F. Muldoon, Cognitive chimera states in human brain networks. *Sci. Adv.* **5**, eaau8535 (2019).
17. A. Arenas, A. Díaz-Guilera, J. Kurths, Y. Moreno, C. Zhou, Synchronization in complex networks. *Phys. Rep.* **469**, 93–153 (2008).
18. M. C. Soriano, J. García-Ojalvo, C. R. Mirasso, I. Fischer, Complex photonics: Dynamics and applications of delay-coupled semiconductors lasers. *Rev. Mod. Phys.* **85**, 421–470 (2013).
19. N. Boers, M. D. Chekroun, H. Liu, D. Kondrashov, D.-D. Rousseau, A. Svensson, M. Bigler, M. Ghil, Inverse stochastic–dynamic models for high-resolution Greenland ice core records. *Earth Syst. Dynam.* **8**, 1171–1190 (2017).
20. A. Keane, B. Krauskopf, C. M. Postlethwaite, Climate models with delay differential equations. *Chaos* **27**, 114309 (2017).
21. S. K. J. Falkena, C. Quinn, J. Sieber, J. Frank, H. A. Dijkstra, Derivation of delay equation climate models using the Mori-Zwanzig formalism. *Proc. R. Soc. A* **475**, 20190075 (2019).
22. K. Gopalsamy, *Stability and Oscillations in Delay Differential Equations of Population Dynamics* (Springer Science & Business Media, 2013), vol. 74.

23. T. Erneux, J. Javaloyes, M. Wolfrum, S. Yanchuk, Introduction to focus issue: Time-delay dynamics. *Chaos* **27**, 114201 (2017).
24. H. Wernecke, B. Sándor, C. Gros, Chaos in time delay systems, an educational review. *Phys. Rep.* **824**, 1–40 (2019).
25. M. D. Chekroun, M. Ghil, J. D. Neelin, Pullback attractor crisis in a delay differential ENSO model, in *Advances in Nonlinear Geosciences*, A. Tsonis, Ed. (Springer, 2018), pp. 1–33.
26. T. Erneux, *Applied Delay Differential Equations* (Springer Science & Business Media, 2009), vol. 3.
27. K. D. Beheng, A parameterization of warm cloud microphysical conversion processes. *Atmos. Res.* **33**, 193–206 (1994).
28. J. W.-B. Lin, J. D. Neelin, Considerations for stochastic convective parameterization. *J. Atmos. Sci.* **59**, 959–975 (2002).
29. J. Berner, U. Achatz, L. Batte, L. Bengtsson, A. Cámara, H. M. Christensen, M. Colangeli, D. R. B. Coleman, D. Crommelin, S. I. Dolaptchiev, C. L. E. Franzke, P. Friederichs, P. Imkeller, H. Järvinen, S. Juricke, V. Kitsios, F. Lott, V. Lucarini, S. Mahajan, T. N. Palmer, Stochastic parameterization: Toward a new view of weather and climate models. *Bull. Am. Meteorol. Soc.* **98**, 565–588 (2017).
30. I. Koren, G. Feingold, Aerosol-cloud-precipitation system as a predator-prey problem. *Proc. Natl. Acad. Sci. U.S.A.* **108**, 12227–12232 (2011).
31. I. Koren, E. Tziperman, G. Feingold, Exploring the nonlinear cloud and rain equation. *Chaos* **27**, 013107 (2017).
32. M. D. Chekroun, I. Koren, H. Liu, Efficient reduction for diagnosing Hopf bifurcation in delay differential systems: Applications to cloud-rain models. *Chaos* **30**, 053130 (2020).
33. H. Xue, G. Feingold, B. Stevens, Aerosol effects on clouds, precipitation, and the organization of shallow cumulus convection. *J. Atmos. Sci.* **65**, 392–406 (2008).
34. H. Wang, G. Feingold, Modeling mesoscale cellular structures and drizzle in marine stratocumulus. Part II: The microphysics and dynamics of the boundary region between open and closed cells. *J. Atmos. Sci.* **66**, 3257–3275 (2009).
35. I. Koren, G. Feingold, Adaptive behavior of marine cellular clouds. *Sci. Rep.* **3**, 2507 (2013).
36. S. Smale, Differentiable dynamical systems. *Bull. Am. Math. Soc.* **73**, 747–817 (1967).
37. J. Guckenheimer, P. Holmes, *Nonlinear Oscillations, Dynamical Systems, and Bifurcations of Vector Fields* (Springer Science & Business Media, 2013), vol. 42.
38. A. Cavagna, A. Cimarelli, I. Giardina, G. Parisi, R. Santagati, F. Stefanini, M. Viale, Scale-free correlations in starling flocks. *Proc. Natl. Acad. Sci. U.S.A.* **107**, 11865–11870 (2010).
39. T. J. Schmit, P. Griffith, M. M. Gunshor, J. M. Daniels, S. J. Goodman, W. J. Lebair, A closer look at the ABI on the GOES-R series. *Bull. Am. Meteorol. Soc.* **98**, 681–698 (2017).
40. S. Lunderman, M. Morzfeld, F. Glassmeier, G. Feingold, Estimating parameters of the nonlinear cloud and rain equation from a large-eddy simulation. *Physica D* **410**, 132500 (2020).
41. W. C. Skamarock, J. B. Klemp, J. Dudhia, D. O. Gill, Z. Liu, J. Berner, W. Wang, J. G. Powers, M. G. Duda, D. M. Barker, X.-Y. Huang, A description of the advanced research WRF model version 4. *National Center for Atmospheric Research (NCAR) Technical Notes*, TN-556+STR, 2021.
42. A. Winfree, Biological rhythms and the behavior of populations of coupled oscillators. *J. Theor. Biol.* **16**, 15–42 (1967).
43. A. Winfree, *The Geometry of Biological Time* (Springer-Verlag, Berlin, 1980).
44. E. A. Coddington, N. Levinson, *Theory of Ordinary Differential Equations* (Tata McGraw-Hill Education, 1955).
45. J. Guckenheimer, Isochrons and phaseless sets. *J. Math. Biol.* **1**, 259–273 (1975).
46. E. M. Izhikevich, *Dynamical Systems in Neuroscience: The Geometry of Excitability and Bursting* (MIT Press, 2010).
47. M. Engel, J. S. W. Lamb, M. Rasmussen, Bifurcation analysis of a stochastically driven limit cycle. *Commun. Math. Phys.* **365**, 935–942 (2019).
48. T. Son Doan, M. Engel, J. S. W. Lamb, M. Rasmussen, Hopf bifurcation with additive noise. *Nonlinearity* **31**, 4567–4601 (2018).
49. J. M. Ottino, *The Kinematics of Mixing: Stretching, Chaos, and Transport* (Cambridge Univ. Press, 1989), vol. 3.
50. M. D. Chekroun, M. Ghil, H. Liu, S. Wang, Low-dimensional Galerkin approximations of nonlinear delay differential equations. *Discrete Continuous Dyn. Syst.* **36**, 4133–4177 (2016).
51. M. D. Chekroun, H. Liu, J. C. McWilliams, Variational approach to closure of nonlinear dynamical systems: Autonomous case. *J. Stat. Phys.* **179**, 1073–1160 (2020).
52. A. Tantet, M. D. Chekroun, H. A. Dijkstra, J. D. Neelin, Ruelle-Pollicott resonances of stochastic systems in reduced state space. Part II: Stochastic Hopf Bifurcation. *J. Stat. Phys.* **179**, 1403–1448 (2020).
53. H. C. Rodean, *Stochastic Lagrangian Models of Turbulent Diffusion* (Springer, 1996), vol. 45.
54. S. N. Stechmann, J. D. Neelin, A stochastic model for the transition to strong convection. *J. Atmos. Sci.* **68**, 2955–2970 (2011).
55. A. J. Majda, S. N. Stechmann, Stochastic models for convective momentum transport. *Proc. Natl. Acad. Sci. U.S.A.* **105**, 17614–17619 (2008).
56. B. Khouider, A. J. Majda, M. A. Katsoulakis, Coarse-grained stochastic models for tropical convection and climate. *Proc. Natl. Acad. Sci. U.S.A.* **100**, 11941–11946 (2003).
57. J. Dorrestijn, D. T. Crommelin, A. P. Siebesma, H. J. J. Jonker, F. Selten, Stochastic convection parameterization with Markov chains in an intermediate-complexity GCM. *J. Atmos. Sci.* **73**, 1367–1382 (2016).
58. N. Chen, A. J. Majda, C. T. Sabeerali, R. S. Ajayamohan, Predicting monsoon intraseasonal precipitation using a low-order nonlinear stochastic model. *J. Climate* **31**, 4403–4427 (2018).
59. A. Bellen, M. Zennaro, *Numerical Methods for Delay Differential Equations* (Oxford Univ. Press, 2013).
60. S. Maset, Numerical solution of retarded functional differential equations as abstract Cauchy problems. *J. Comput. Appl. Math.* **161**, 259–282 (2003).
61. A. Bellen, S. Maset, Numerical solution of constant coefficient linear delay differential equations as abstract Cauchy problems. *Numer. Math.* **84**, 351–374 (2000).
62. S. Yanchuk, G. Giacomelli, Spatio-temporal phenomena in complex systems with time delays. *J. Phys. A Math. Theor.* **50**, 103001 (2017).
63. F. T. Arecchi, G. Giacomelli, A. Lapucci, R. Meucci, Two-dimensional representation of a delayed dynamical system. *Phys. Rev. A* **45**, R4225–R4228 (1992).
64. H. Aref, Stirring by chaotic advection. *J. Fluid Mech.* **143**, 1–21 (1984).
65. J. M. Ottino, S. C. Jana, V. S. Chakravarthy, From Reynolds's stretching and folding to mixing studies using horseshoe maps. *Phys. Fluids* **6**, 685–699 (1994).
66. K. Wójcik, P. Zgliczyński, Topological horseshoes and delay differential equations. *Discrete Continuous Dyn. Syst.* **12**, 827–852 (2005).
67. C. Feng, H. Zhao, Random periodic processes, periodic measures and ergodicity. *J. Differ. Equ.* **269**, 7382–7428 (2020).
68. O. E. Rossler, An equation for hyperchaos. *Phys. Lett. A* **71**, 155–157 (1979).
69. G. Baier, S. Sahle, Design of hyperchaotic flows. *Phys. Rev. E* **51**, R2712–R2714 (1995).
70. M. D. Chekroun, J. D. Neelin, D. Kondrashov, J. C. McWilliams, M. Ghil, Rough parameter dependence in climate models and the role of Ruelle-Pollicott resonances. *Proc. Natl. Acad. Sci. U.S.A.* **111**, 1684–1690 (2014).
71. M. D. Chekroun, A. Tantet, H. A. Dijkstra, J. D. Neelin, Ruelle–Pollicott resonances of stochastic systems in reduced state space. Part I: Theory. *J. Stat. Phys.* **179**, 1366–1402 (2020).
72. T. Dror, V. Silverman, O. Altaratz, M. D. Chekroun, I. Koren, Uncovering the large-scale meteorology that drives continental, shallow, green cumulus through supervised classification. *Geophys. Res. Lett.* **49**, e2021GL096684 (2022).
73. R. Wood, Stratocumulus clouds. *Mon. Weather Rev.* **140**, 2373–2423 (2012).
74. A. Guillamon, G. Huguet, A computational and geometric approach to phase resetting curves and surfaces. *SIAM J. Appl. Dyn. Syst.* **8**, 1005–1042 (2009).
75. A. Mauroy, B. Rhoads, J. Moehlis, I. Mezic, Global isochrons and phase sensitivity of bursting neurons. *SIAM J. Appl. Dyn. Syst.* **13**, 306–338 (2014).
76. M. Detrixhe, M. Doubeck, J. Moehlis, F. Gibou, A fast Eulerian approach for computation of global isochrons in high dimensions. *SIAM J. Appl. Dyn. Syst.* **15**, 1501–1527 (2016).
77. M. J. Panaggio, D. M. Abrams, Chimera states: Coexistence of coherence and incoherence in networks of coupled oscillators. *Nonlinearity* **28**, R67 (2015).
78. J. M. Gomes, R. Weber dos Santos, E. M. Cherry, Alternans promotion in cardiac electrophysiology models by delay differential equations. *Chaos* **27**, 093915 (2017).
79. K. H. W. J. ten Tusscher, D. Noble, P.-J. Noble, A. V. Panfilov, A model for human ventricular tissue. *Am. J. Physiol. Heart Circ. Phys.* **286**, H1573–H1589 (2004).
80. J. E. Marsden, M. McCracken, *The Hopf Bifurcation and Its Applications* (Springer Science & Business Media, 2012), vol. 19.
81. T. Ma, S. Wang. *Phase Transition Dynamics* (Springer, 2014).
82. D. Kondrashov, M. D. Chekroun, P. Berloff, Multiscale Stuart-Landau emulators: Application to wind-driven ocean gyres. *Fluids* **3**, 21 (2018).
83. M. D. Chekroun, H. Liu, J. C. McWilliams, Stochastic rectification of fast oscillations on slow manifold closures. *Proc. Natl. Acad. Sci. U.S.A.* **118**, e2113650118 (2021).
84. G. Thompson, T. Eidhammer, A study of aerosol impacts on clouds and precipitation development in a large winter cyclone. *J. Atmos. Sci.* **71**, 3636–3658 (2014).
85. S.-Y. Hong, Y. Noh, J. Dudhia, A new vertical diffusion package with an explicit treatment of entrainment processes. *Mon. Weather Rev.* **134**, 2318–2341 (2006).
86. P. A. Jiménez, J. Dudhia, J. F. González-Rouco, J. Navarro, J. P. Montávez, E. García-Bustamante, A revised scheme for the WRF surface layer formulation. *Mon. Weather Rev.* **140**, 898–918 (2012).
87. K. Engelborghs, T. Luzyanina, D. Roose, Numerical bifurcation analysis of delay differential equations using DDE-BIFTOOL. *ACM Trans. Math. Softw.* **28**, 1–21 (2002).
88. R. B. Vinter, On the evolution of the state of linear differential delay equations in M^2: Properties of the generator. *IMA J. Appl. Math.* **21**, 13–23 (1978).

Acknowledgments: The insights discussed in this work have substantially benefited from the reviewers' constructive comments, and we thus express our deep gratitude to them. **Funding:** This work has been partially supported by the European Research Council (ERC) under the European Union's Horizon 2020 research and innovation program (grant agreement no. 810370), by the National Science Foundation grant DMS-2108856, and by the Office of Naval Research (ONR) Multidisciplinary University Research Initiative (MURI) grant N00014-20-1-2023. This study was also supported by a Ben May Center grant for theoretical and/or computational research and by the Israeli Council for Higher Education (CHE) via the Weizmann Data Science Research Center. We also acknowledge the computational resources provided by Advanced Research Computing at Virginia Tech. **Author contributions:** This work initiated from discussions between M.D.C. and I.K. M.D.C. conceptualized the approach. M.D.C. and Honghu Liu conceptualized the mathematical and algorithmic details. Honghu Liu performed the numerical implementations for the stochastic transport problems assisted by M.D.C. for data analysis and low-order models analysis, while Huan Liu conducted the WRF simulations under supervision of I.K. M.D.C., I.K., and Honghu Liu interpreted the main results and wrote the manuscript. **Competing interests:** The authors declare that they have no competing interests. **Data and materials availability:** All data needed to evaluate the conclusions in the paper are present in the paper and/or the Supplementary Materials.

Submitted 26 April 2022
Accepted 17 October 2022
Published 18 November 2022
10.1126/sciadv.abq7137

ScienceAdvances

Generic generation of noise-driven chaos in stochastic time delay systems: Bridging the gap with high-end simulations

Mickaël D. ChekrounIlan KorenHonghu LiuHuan Liu

Sci. Adv., 8 (46), eabq7137. • DOI: 10.1126/sciadv.abq7137

Science Advances (ISSN) is published by the American Association for the Advancement of Science. 1200 New York Avenue NW, Washington, DC 20005. The title *Science Advances* is a registered trademark of AAAS.

Science Advances
AAAS

Supplementary Materials for

Generic generation of noise-driven chaos in stochastic time delay systems: Bridging the gap with high-end simulations

Mickaël D. Chekroun *et al.*

Corresponding author: Mickaël D. Chekroun, michael-david.chekroun@weizmann.ac.il

Sci. Adv. **8**, eabq7137 (2022)
DOI: 10.1126/sciadv.abq7137

The PDF file includes:

Other Supplementary Material for this manuscript includes the following:

Supplementary Note 1

Shear-induced chaos from Eq. (7) of the Main Text. As shown in Fig. 1, the stochastic Stuart-Landau (SL) equation *Eq. (7) of the Main Text* perturbed by the state-dependent random forcing $F(t,z)$ given by *Eq. (6) of the Main Text*, exhibits shear-induced chaos when the parameters f_r, D and σ involved in $F(t,z)$ are suitably chosen; cf. Fig. 1 (B and C). There, two snapshots of the pullback attractor, $\mathcal{A}(t)$, are shown at times $t = 68$ and $t = 78$, exhibiting stretching and folding for $D = 60$ and $\sigma = 0.1$. In this figure, two nearby points are marked as red and cyan dots on the pullback attractor shown at $t = 68$ (Fig. 1B) which correspond to trajectories driven by the same noise path that have synchronised at that time (dashed vertical line in Fig. 1A prior $t \approx 70$). This synchronisation holds for a certain time-window before breaking down (while still driven by the same noise path) at a later time (dashed vertical line in Fig. 1A prior $t \approx 80$), illustrating the sensitive dependence on initial conditions (compare Fig. 1B with Fig. 1C), signature of chaotic dynamics. This on-off synchronisation behaviour repeats in the course of time as already visible in Fig. 1A; a feature also encountered for other types of noise-driven chaos as documented in e.g. [4, Fig. 7].

Supplementary Note 2

We recall briefly here the transport equation reformulation of the Koren-Tziperman-Feingold (KTF) model delay model [31,32], and also point out how the Stuart-Landau (SL) equation is obtained as the normal form of Galerkin–Koornwinder (GK) approximations of this model [32].

Transport equation reformulation. Recall the KTF model rewritten for the perturbed variable, $H(t) = h(t) - \bar{h}$:

$$\dot{H} = -H(t) - \frac{2}{\mu}\bar{h}\, H(t-\tau) - \frac{1}{\mu}H^2(t-\tau). \qquad \textbf{(S1)}$$

Denote by $u(t,\theta)$ the historic part of H, that is $u(t,\theta) = H(t+\theta)$ for θ in $[-\tau, 0)$. Recall that the transport equation reformulation of Eq. (S1) is given by

$$\partial_t u = \partial_\theta u, \qquad \textbf{(S2)}$$

subject to the boundary conditions

$$\partial_\theta u|_{\theta=0} = -u(t,0) - \frac{2}{\mu}\bar{h}u(t,-\tau) - \frac{1}{\mu}u^2(t,-\tau). \qquad \textbf{(S3)}$$

We introduce next the linear operator A acting on $\Phi = (\phi, \phi(0))$ (with suitable regularity on the function ϕ over $[-\tau, 0]$; see [50])

$$[A\Phi](\theta) = \begin{cases} \dfrac{\mathrm{d}\phi}{\mathrm{d}\theta}, & \theta \in [-\tau, 0), \\ -\phi(0) - \frac{2}{\mu}\bar{h}\,\phi(-\tau), & \theta = 0. \end{cases} \qquad \textbf{(S4)}$$

By introducing finally the nonlinear operator G

$$[G\Phi](\theta) = \begin{cases} 0, & \theta \in [-\tau, 0), \\ -\dfrac{1}{\mu}\phi^2(-\tau), & \theta = 0, \end{cases} \qquad \textbf{(S5)}$$

we can rewrite the boundary problem (S2)-(S3) as the following abstract evolution equation defined on a suitable Hilbert function space (see e.g. [50, Sec. 2])

$$\frac{\mathrm{d}u}{\mathrm{d}t} = Au + G(u). \qquad \textbf{(S6)}$$

GK approximations and Hopf normal form. Recall that the forcing—aimed at turning a limit cycle into a stochastic strange attractor—is designed from the SL equation, *Eq. (4) of the Main Text*. We succinctly recall below its derivation. Following [32], the SL equation is the Hopf normal form associated with the loss of stability of the unstable mode $\boldsymbol{e}_1^N$ of an N-dimensional GK approximation of the KTF model, with N sufficiently large.

Such Galerkin approximations are obtained from Eq. (S6) as

$$\frac{\mathrm{d}\boldsymbol{y}_N}{\mathrm{d}t} = \Gamma_N(\tau)\boldsymbol{y}_N + G_N(\boldsymbol{y}_N), \qquad \boldsymbol{y}_N \in \mathbb{R}^N, \qquad \textbf{(S7)}$$

in which the $N \times N$ matrix $\Gamma_N(\tau)$ (resp. G_N) results from the truncation of the operator A (resp. $G(u)$) to the N-dimensional subspace associated with the first N Koornwinder polynomials over $[-\tau, 0]$, while $\boldsymbol{y}_N$ provides the (time-dependent) coefficients of this Galerkin approximation of $u(t,\theta)$ within this subspace; see [32, Eq. (45)–(48)] and [50, Sec. 5].

By rewriting the GK system Eq. (S7) under the eigenmodes of $\Gamma_N(\tau)$, we obtain

$$\frac{\mathrm{d}z_k}{\mathrm{d}t} = \lambda_k^N z_k + \Big\langle G_N\Big(\sum_{j=1}^N z_j \boldsymbol{e}_j^N\Big), \widehat{\boldsymbol{e}}_k^N \Big\rangle,\ k = 1, \cdots, N, \tag{S8}$$

where $(\lambda_j^N, \boldsymbol{e}_j^N)$ denotes the eigenelements of $\Gamma_N(\tau)$ and $(\widehat{\lambda}_j^N, \widehat{\boldsymbol{e}}_j^N)$ those of the transpose of $\Gamma_N(\tau)$. The SL equation

$$\frac{\mathrm{d}z}{\mathrm{d}t} = \lambda_1^N z - (\alpha_N + i\beta_N) z|z|^2, \tag{S9}$$

is finally obtained from Eq. (S8) by application of the approximation formulas of the center manifold following [51 ,Sec. 2.2]; see [32, Theorem III.1].

Supplementary Note 3

Stochastic transport problem: Murmuration case

We consider here the case when the forcing, $F(t)$, is independent of the state itself i.e. corresponding to the murmuration case in the *Main Text*. Our goal is to make precise how to lift a stochastic forcing of the SL equation (*Eq. (4) of the Main Text*) into a stochastic forcing of the corresponding KTF transport equation formulation.

As recalled above, the SL equation (S9) is here derived from the loss of stability of the unstable mode $\boldsymbol{e}_1^N$ of a sufficiently high-dimensional GK approximation of the KTF model and provides, near criticality, a rigorous approximation of the unstable mode's amplitude [32, Theorem III.1]. Thus the idea of "lifting" a forcing of the SL equation (S9) into a forcing of the unstable mode in the GK system, while expecting a similar dynamical response to such perturbations than in the case of the SL equation.

By adding a forcing $F(t)$ to Eq. (S8) we consider therefore the following forced version of the GK system:

$$\begin{aligned}
\frac{\mathrm{d}z_1}{\mathrm{d}t} &= \lambda_1^N z_1 + \Big\langle G_N\Big(\sum_{j=1}^N z_j \boldsymbol{e}_j^N\Big), \widehat{\boldsymbol{e}}_1^N \Big\rangle + F(t),\\
\frac{\mathrm{d}z_2}{\mathrm{d}t} &= (\lambda_1^N)^* z_2 + \Big\langle G_N\Big(\sum_{j=1}^N z_j \boldsymbol{e}_j^N\Big), \widehat{\boldsymbol{e}}_2^N \Big\rangle + F^*(t),
\end{aligned} \tag{S10}$$

and for $k = 3, \cdots, N$,

$$\frac{\mathrm{d}z_k}{\mathrm{d}t} = \lambda_k^N z_k + \Big\langle G_N\Big(\sum_{j=1}^N z_j \boldsymbol{e}_j^N\Big), \widehat{\boldsymbol{e}}_k^N \Big\rangle.$$

Note the use of complex conjugates $F^*(t)$ and $(\lambda_1^N)^*$ in the z_1- and z_2-equations of Eq. (S10). The reason is as follows. To proceed, recall that the GK system is placed after a Hopf bifurcation has occurred and hence the unstable mode $\boldsymbol{e}_1^N$ is associated with an unstable pair of complex eigenvalues. Thus forcing this mode leads to force its amplitude equation (the z_1-equation) and the equation for its conjugate amplitude (the z_2-equation).

Using $\boldsymbol{y}_N = \sum_{j=1}^N z_j \boldsymbol{e}_j^N$, we can rewrite (S10) into the compact form [50, Sec. 5]

$$\frac{\mathrm{d}\boldsymbol{y}_N}{\mathrm{d}t} = \Gamma_N(\tau)\boldsymbol{y}_N + G_N(\boldsymbol{y}_N) + \boldsymbol{F}_N(t), \tag{S11}$$

where

$$\boldsymbol{F}_N(t) = F(t)\boldsymbol{e}_1^N + F^*(t)\boldsymbol{e}_2^N = F(t)\boldsymbol{e}_1^N + \text{ c.c.}, \tag{S12}$$

with c.c. denoting the complex conjugate of the immediate term preceding the "+" sign.

Denoting by K_j^τ the (rescaled) Koornwinder polynomials used for the Galerkin approximation following [32, 50], the function $u_N(t,\theta) = \sum_{j=1}^N \boldsymbol{y}_N^j(t) K_j^\tau(\theta)$ approximates then the solution $u(t,\theta)$ of the abstract evolution equation (S6); see [32, Sec. II.C]. The forcing $\boldsymbol{F}_N(t)$ translates in this format into the function

$$f_N(t,\theta) = \sum_{j=1}^N F_N^j(t) K_j^\tau(\theta) = \sum_{j=1}^N F(t) e_{1,j}^N K_j^\tau(\theta) + \text{ c.c.}, \tag{S13}$$

in which $F_N^j(t)$ (resp. $e_{1,j}^N$) denotes the j-th component (in $\mathbb{R}^N$) of the N-dimensional vector $\boldsymbol{F}_N(t)$ (resp. of the dominant eigenmode $\boldsymbol{e}_1^N$ of $\Gamma_N(\tau)$). In (S13), $F_N^j(t)$ is also interpretable as the j-th coefficient of $f_N(t,\theta)$ onto the Koornwinder basis.

Using the Koornwinder polynomials, the eigenvector, $\boldsymbol{e}_1^N$, has the following representation in the θ-variable:

$$\varphi_1^N(\theta) = \sum_{j=1}^N e_{1,j}^N K_j^\tau(\theta),\ \theta \in [-\tau, 0], \tag{S14}$$

and in particular $f_N(t,\theta)$ simply becomes

$$f_N(t,\theta) = F(t)\varphi_1^N(\theta). \tag{S15}$$

We are then only left with determining the function towards which $f_N(t,\theta)$ converges as $N \to \infty$, in order to conclude about the forcing term to add to the right-hand side of (S6).

Denoting by (λ_1, φ_1) the leading eigenpair of the linear operator A, we have then that $(\lambda_1^N, \varphi_1^N)$ converges, as $N \to \infty$, towards (λ_1, φ_1), with

$$\varphi_1^N \xrightarrow[N\to\infty]{L^2} \varphi_1,$$

where "$\xrightarrow{L^2}$" denotes the convergence for the norm associated with the inner product given by *Eq. (16) of the Main Text*.

The rigorous proof of this convergence goes beyond the scope of this article. Supplementary Figures 2–3 provide nevertheless numerical results supporting this convergence.

These results of numerical convergence of $f_N(t,\theta)$ towards $F(t)\varphi_1 + \text{c.c.}$ (in a mean-square sense) lead us to conclude that the limiting problem, as $N \to \infty$, corresponds to the following forced evolution equation

$$\frac{\mathrm{d}u}{\mathrm{d}t} = \big(Au + G(u)\big) + \Big(F(t)\varphi_1 + \text{c.c.}\Big), \tag{S16}$$

with A and G as defined in (S4) and (S5), respectively.

The latter equation rewrites as the following stochastic transport problem

$$\partial_t u = \partial_\theta u + \Big(F(t)\varphi_1 + \text{c.c.}\Big),\ \theta \in [-\tau, 0), \tag{S17}$$

subject to the boundary conditions

$$\begin{aligned}\partial_t u|_{\theta=0} = -u(t,0) - \frac{2}{\mu}\bar{h}u(t,-\tau) - \frac{1}{\mu}u^2(t,-\tau) \\ + \Big(F(t)\varphi_1(0) + \text{c.c.}\Big).\end{aligned} \tag{S18}$$

Now by taking $\theta = 0$ in (S17) (via a continuity argument), one gets $\partial_t u|_{\theta=0} = \partial_\theta u|_{\theta=0} + \Big(F(t)\varphi_1(0) + \text{c.c.}\Big)$ and by expressing $\partial_t u|_{\theta=0}$ using (S18) one obtains

$$\partial_\theta u|_{\theta=0} = -u(t,0) - \frac{2}{\mu}\bar{h}u(t,-\tau) - \frac{1}{\mu}u^2(t,-\tau). \tag{S19}$$

Eq. (S17) together with the boundary condition (S19) provides then the stochastic transport problem for the murmuration case analyzed in the *Main Text*. Supplementary Fig. 5 below shows the differences between the murmuration and the horseshoes cases as measured in terms of fluxes at the boundary and within the domain; see the Section *'Noise transmission, fluxes, and murmuration cascade' in the Main Text* for more details.

Supplementary Fig. 9C shows a solution $u(t,\theta)$ to such a stochastic transport problem (*Eqns. (9)-(10) in the Main Text*), along with its time-dependent boundary value $u(t,0)$ at $\theta = 0$ (Supplementary Fig. 9D), providing a stochastic path $H(t)$ (*Eq. (11) in the Main Text*).

Supplementary Note 4

For our calculations, as reported in the *Main Text*, the dominant eigenfunction φ_1 is approximated by φ_1^N according to (S14) with $N = 20$. Note that with $N = 10$ a high-precision (of order 10^{-8}) is already reached by evaluating the corresponding residual; see Supplementary Fig. 3. This is also supported by a simple energy distribution analysis onto the first few Koornwinder polynomials. In that respect, Supplementary Fig. 4 shows the energy distribution of the first eigenfunction φ_1 used to force the transport problem (S17)-(S19). From this distribution, one observes indeed that only the first two Koornwinder polynomials capture most of the energy contained in φ_1, which in other words corresponds to a large-scale forcing. Dynamically, this property means that the results of the *Main Text* are essentially unchanged qualitatively if only a low-order (Koornwinder) approximation of φ_1 is used in the corresponding experiments.

Supplementary Note 5

Stochastic transport problem: Horseshoes case

The derivation of the stochastic transport problem in the case where F is the state-dependent noise (horseshoes case), $F(t,z) = iDf(t)z|z|^2 + \sigma\dot{W}(t)$ (see *Eq. (6) of the Main Text*) follows the same steps in which $f_N(t,\theta)$ in (S15) is now replaced by

$$f_N(t,\theta) = \sum_{j=1}^{N} F(t, \langle \boldsymbol{y}_N, \widehat{\boldsymbol{e}}_1^N\rangle) e_{1,j}^N K_j^\tau + \text{ c.c.}, \tag{S20}$$

where, we recall $\widehat{\boldsymbol{e}}_1^N$ denotes the first eigenvector of the transpose of $\Gamma_N(\tau)$.

At a first glance, denoting by $\widehat{\varphi}_1$ the first eigenvector of the adjoint operator A^*, a formal limit as $N \to \infty$ should lead to an analogue to (S16), namely

$$\frac{\mathrm{d}u}{\mathrm{d}t} = \big(Au + G(u)\big) + \Big(F\big(t, \langle u, \widehat{\varphi}_1\rangle\big)\varphi_1 + \text{c.c.}\Big). \tag{S21}$$

Let $\widehat{\varphi}_1^N$ be the analogue of φ_1^N given by (S14) in which $\boldsymbol{e}_1^N$ is replaced by $\widehat{\boldsymbol{e}}_1^N$. To fully justify (S21), it is sufficient to have weak convergence of $\widehat{\varphi}_1^N$ towards $\widehat{\varphi}_1$ in the sense that $\langle u, \widehat{\varphi}_1^N\rangle$ converges towards $\langle u, \widehat{\varphi}_1\rangle$. Here again, such a convergence analysis goes beyond the scope of this work, and instead numerical evidences are provided in Supplementary Fig. 6A for the unforced KTF model.

Analytic expression of $\widehat{\varphi}_1$ can be obtained for the KTF model; see (S23) below. In this case, the adjoint operator A^* is given for each $\Phi = (\phi, x)$ (for suitable function ϕ on $[-\tau, 0)$ and point-value x at $\theta = 0$ [88] by

$$[A^*\Phi](\theta) = \begin{cases} -\dfrac{\mathrm{d}\phi}{\mathrm{d}\theta}, & \theta \in [-\tau, 0), \\ -x + \phi(0), & \theta = 0. \end{cases} \tag{S22}$$

See e.g. [88, Theorem 5.2].

The first eigenfunction is then given by $\widehat{\varphi}_1 = (\widehat{\varphi}_1^D, \widehat{\varphi}_1^S)$, with

$$\begin{aligned}\widehat{\varphi}_1^D(\theta) &= \alpha \exp(-\lambda_1^*\theta), \quad \theta \in [-\tau, 0), \\ \widehat{\varphi}_1^S &= -\frac{\alpha\mu}{2\bar{h}} \exp(\lambda_1^*\tau),\end{aligned} \tag{S23}$$

where α is an arbitrary non-zero complex-valued constant.

In general however analytic formulas for $\widehat{\varphi}_1$ are not always accessible, and unlike for φ_1, (strong) approximation of $\widehat{\varphi}_1$ by Koornwinder polynomials is not guaranteed to hold. For instance, $\widehat{\varphi}_1$ exhibits typically discontinuities at the boundary $\theta = 0$ (see (S23) for the KTF model) causing spurious Gibbs phenomenon that manifests when attempting to approximate $\widehat{\varphi}_1$ by smooth polynomials. This generic behaviour is tied to the domain $D(A^*)$ of A^*. Recall that like φ_1, the (adjoint) eigenmode $\widehat{\varphi}_1$ is of the form $\widehat{\varphi}_1 = (\phi, x)$ with x a point-value. For $\widehat{\varphi}_1$ to lie in $D(A^*)$ it imposes that x is proportional to $\phi(-\tau)$ which in general does not coincide with $\phi(0)$, causing thus a discontinuity at $\theta = 0$ for $\widehat{\varphi}_1$; see [88, Theorem 5.2].

We then need to rely on high-precision approximation schemes of A^* to compute $\widehat{\varphi}_1$ and the corresponding inner product $\langle u, \widehat{\varphi}_1\rangle$, involving quadrature techniques over a fine meshing, becomes cumbersome to compute at each time step. This constitutes a serious numerical constraint for computing snapshot attractors over a large ensemble of initial data from direct integration of (S21).

On the other hand, φ_1 can be approximated to a very high precision in terms of expansion over a few Koornwinder polynomials; see Supplementary Fig. 3 again for the KTF model. Such a low-dimensional approximation using a few Koornwinder polynomials (see (S14)) reduces the numerical burden of computing the inner product $\langle u, \varphi_1\rangle$, by allowing for a coarser mesh to perform the required quadratures. Naturally,

these observations led us to ask what would be the consequences in dynamical terms of replacing the cumbersome term to compute, $\langle u, \widehat{\varphi}_1 \rangle$ in (**S21**), by the term $\langle u, \varphi_1 \rangle$ and thus by its high-precision approximation $\langle u, \varphi_1^N \rangle$ with N not too large?

Dynamically, such a substitution means that we replace the state-dependent part of the forcing, $iDf(t)\langle u, \widehat{\varphi}_1 \rangle |\langle u, \widehat{\varphi}_1 \rangle|^2$ by $iDf(t)\langle u, \varphi_1 \rangle |\langle u, \varphi_1 \rangle|^2$. Since the purpose of this state-dependent term is to enhance phase diffusion, it is reasonable to expect that the proposed replacement would not affect much the ability of the forced model to generate horseshoes if the phase of $\hat{z}_1 = \langle u, \widehat{\varphi}_1 \rangle$ and that of $z_1 = \langle u, \varphi_1 \rangle$ are relatively close to each other, i.e. if z_1 and $\hat{z}_1$ evolves in a nearly synchronous manner. To measure the level of coherence between these oscillating variables we employ the following complex order parameter [43]

$$r(t)e^{i\psi(t)} = (e^{i \arg(z_1(t))} + e^{i \arg(\hat{z}_1(t))})/2, \qquad \textbf{(S24)}$$

where $r(t)$ in $[0, 1]$ is the modulus and $\psi(t)$ is the phase of the considered indicator. This indicator when computed for the unperturbed dynamics of the KTF model, reveals that z_1 and $\hat{z}_1$ are nearly synchronised as $r(t)$ remains very close to 1 in the course of time; see Supplementary Fig. 6B. We already reported abundantly in the *Main Text* that (**S21**) with $\langle u, \widehat{\varphi}_1 \rangle$ replaced by $\langle u, \varphi_1 \rangle$ led to the creation of horseshoes in the state-space for the right choice of parameters. Supplementary Fig. 7 below provides a few examples of such parameter-values leading to time-variability associated with stochastic horseshoes (Panels (C)-(D) and (E)-(F)).

Qualitatively, (**S21**) exhibits still horseshoes dynamics when $\langle u, \widehat{\varphi}_1 \rangle$ is used in the latter equation (see Supplementary Fig. 6C) supporting thus on a dynamical ground our choice motivated by the aforementioned numerical considerations regarding the use of $\langle u, \varphi_1 \rangle$ address state-dependence of the noise. We believe that this observation of preserving qualitatively the effects of a state-dependent forcing compared to another one when their phases are nearly synchronised is not limited to the KTF model and should hold for more general systems.

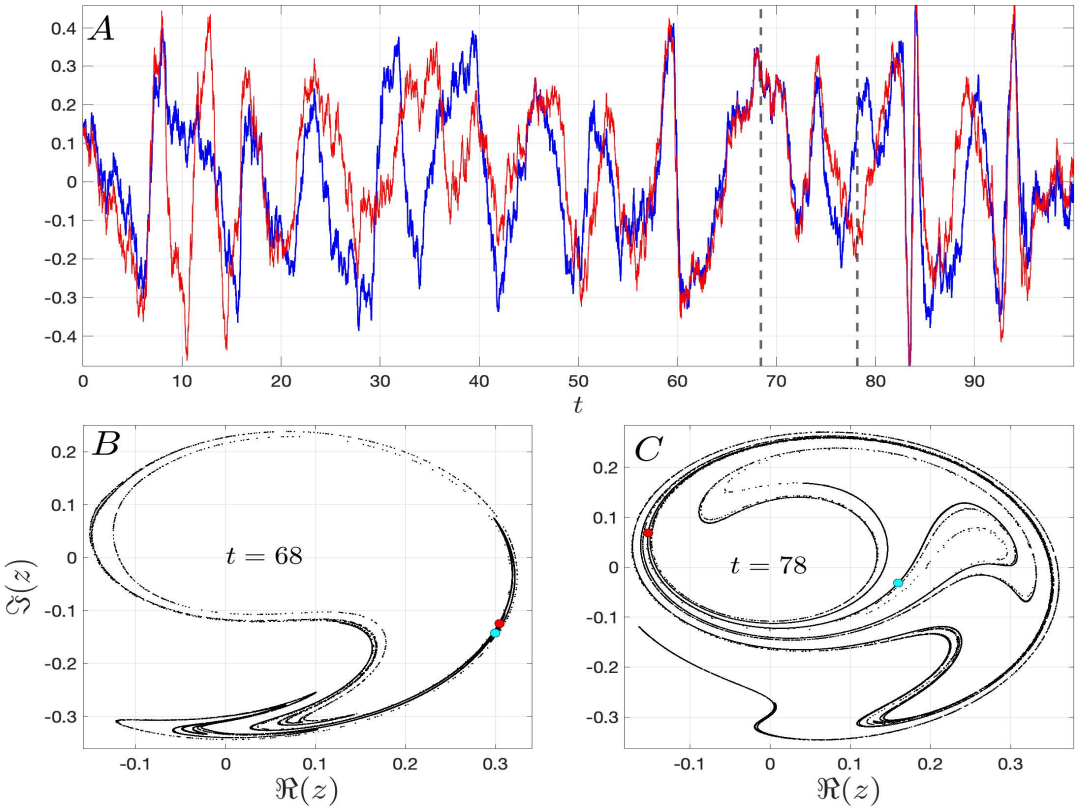

Supplementary Fig. 1: **Shear-induced chaos from Eq. (7) of the Main Text.** Here, F is the state-dependent random forcing as in *Eq. (6) of the Main Text* while λ_1^N, α_N, and β_N are as given in the *caption of Fig. 10 of the Main Text*. The snapshot attractors shown in (**B** and **C**) correspond to the time frames marked by the dashed vertical lines in (**A**). The red dots in (B) and (C) correspond to the stochastic trajectory ($\Re z(t)$) shown in red in panel A while the cyan dots to that shown in blue. These trajectories are driven by a same noise path with $D = 60$, $\sigma = 0.1$ and firing rate $f_r = 0.7$ in *Eq. (6) of the Main Text*.

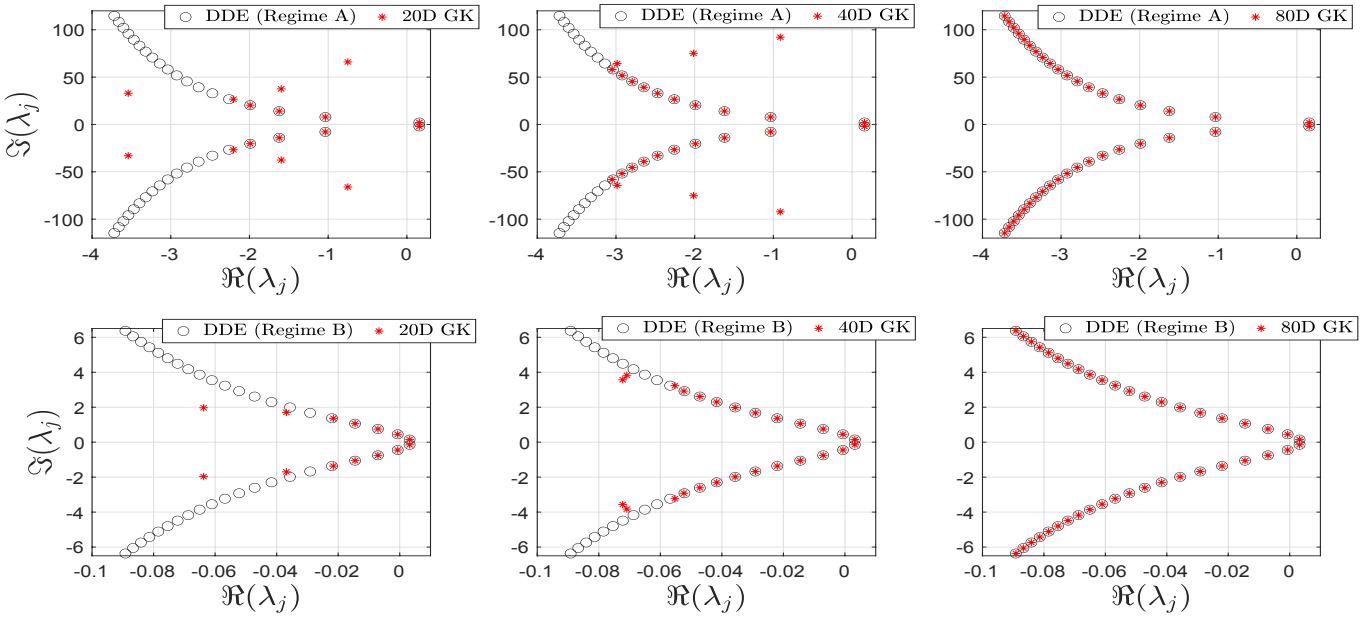

Supplementary Fig. 2: **Convergence, as N increases, of the eigenvalues λ_j^N (red asterisks) of the truncated operator $\Gamma_N(\tau)$ in (S7), towards those of the operator A defined in (S4) (black circles)**. The reference eigenvalues are obtained by solving the characteristic equation $\lambda + 1 + \frac{2}{\mu}\bar{h}\,\exp(-\tau\lambda) = 0$ using the DDE-BIFTOOL Matlab package [87]. The top row corresponds to KTF model's parameters, $\mu = 0.3$ and $\tau = 1$ (Regime A), while the bottom row corresponds to $\mu = 1.2$ and $\tau = 20$ (Regime B). Note that the spectral gap, along the real axis, between the unstable pair and the immediate stable one gets much smaller in Regime B than in Regime A. This phenomenon has consequences for application of the center manifold reduction techniques; see the Section *'Response dependence to stochastic parameterization' of the Main Text.*

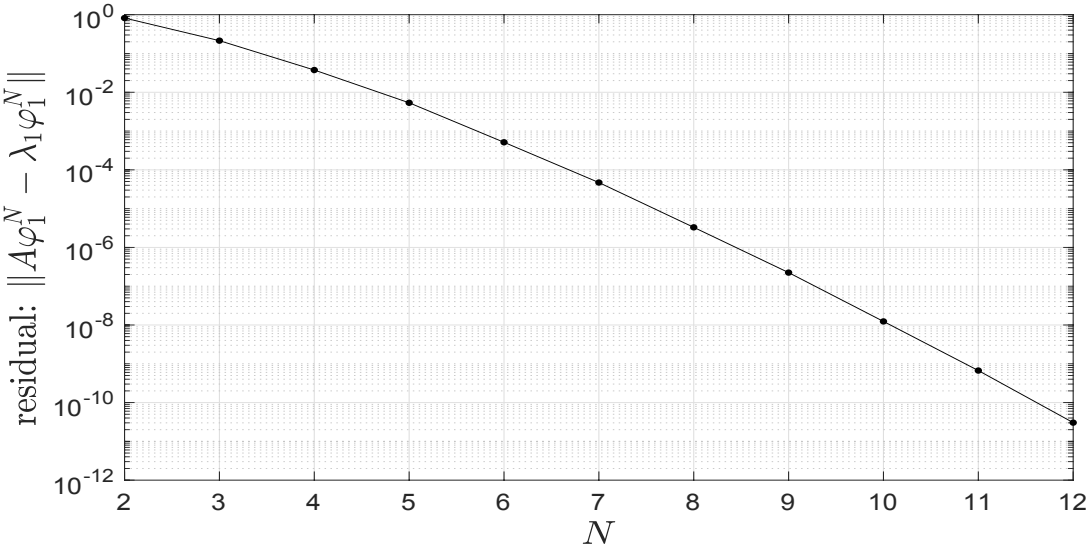

Supplementary Fig. 3: **Residual error of φ_1^N given by (S14) in approximating the first eigenfunction φ_1 of the linear operator A.** Here, φ_1^N is obtained according to (S14), from the first eigenmode $\boldsymbol{e}_1^N$ of the $N \times N$ matrix $\Gamma_N(\tau)$ in (S7). To evaluate the error $\|A\varphi_1^N - \lambda_1\varphi_1^N\|$, we use the analytic formulas for the derivative of Koornwinder polynomials (see Proposition A.1 in [32]) allowing for reaching high-precision in evaluating $A\varphi_1^N$ while λ_1 is obtained as the dominant eigenvalue of A using the DDE-BIFTOOL Matlab package [87]. Note that already with $N = 10$ Koornwinder polynomials a precision of order 10^{-8} is reached in approximating by φ_1^N the genuine dominant mode, φ_1, of A. These convergence results are shown here for Regime A, i.e., $\mu = 0.3$ and $\tau = 1$, as an illustration.

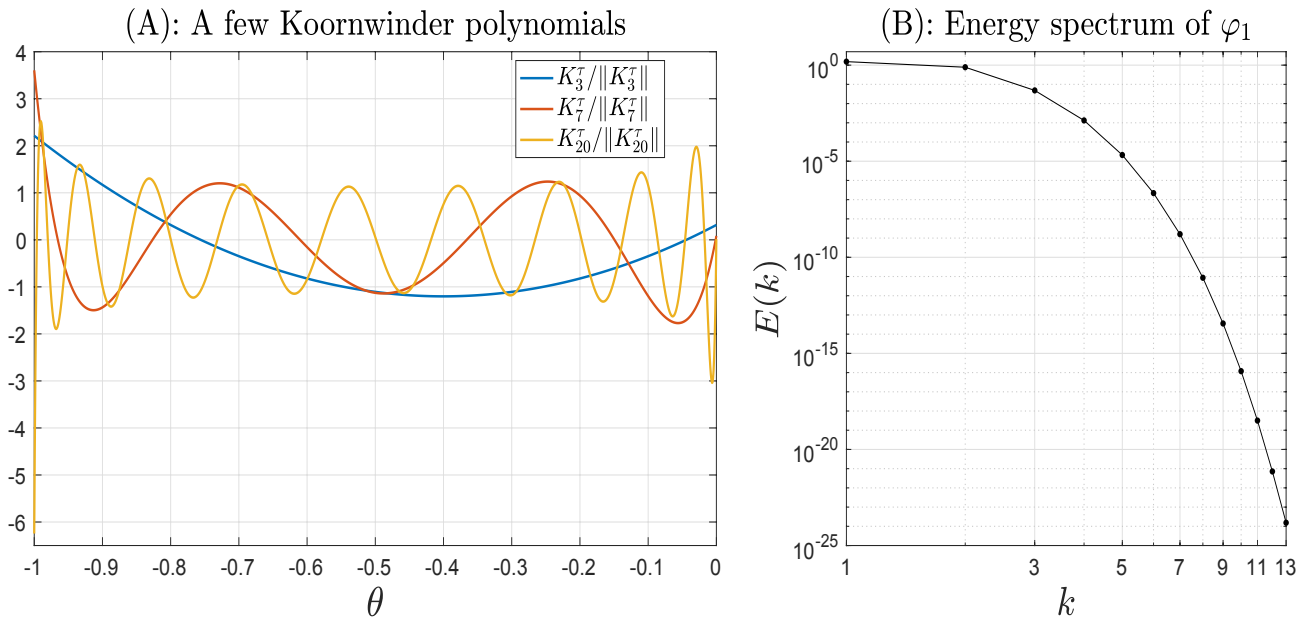

Supplementary Fig. 4: **Koornwinder polynomials and energy distribution of the first eigenfunction, φ_1, against the first few Koornwinder polynomials**. (**A**) A few (normalized) Koornwinder polynomials. (**B**) Energy distribution of the first eigenfunction φ_1 used to force the transport problem (S17)-(S19), onto the first few Koornwinder polynomials; see also "Supplementary Note 4." It shows that φ_1 corresponds to a large-scale perturbation in Eq. (10) of the Main Text.

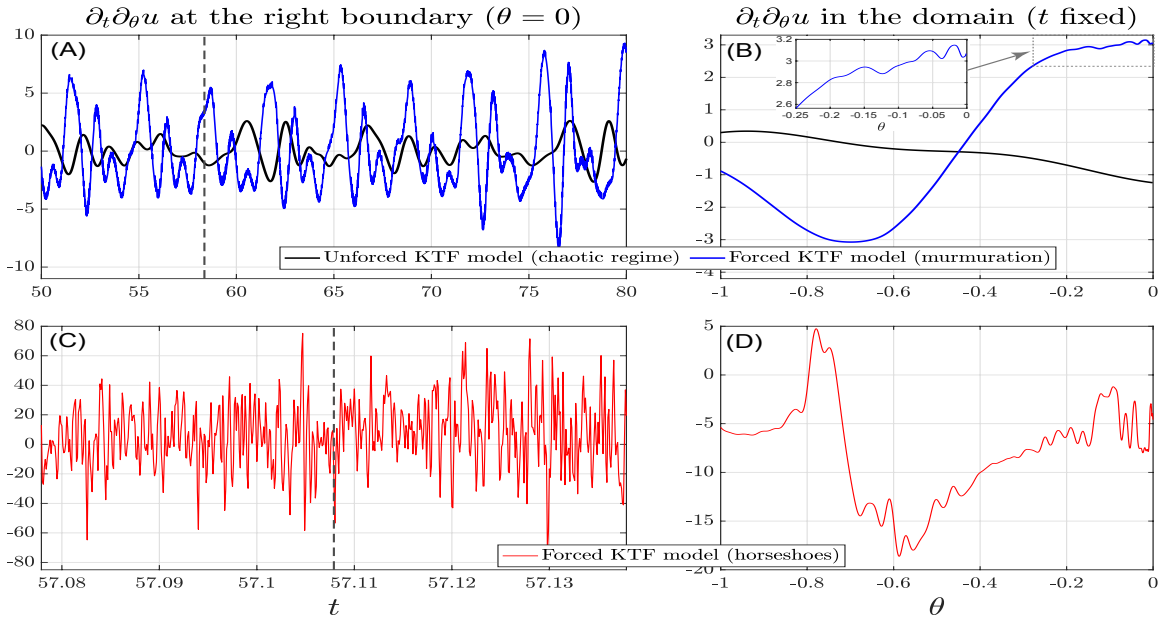

Supplementary Fig. 5: **Fluxes, $\mathfrak{F}(t,\theta) = \partial_t\partial_\theta u$, at the boundary and within the domain**. See Main Text.

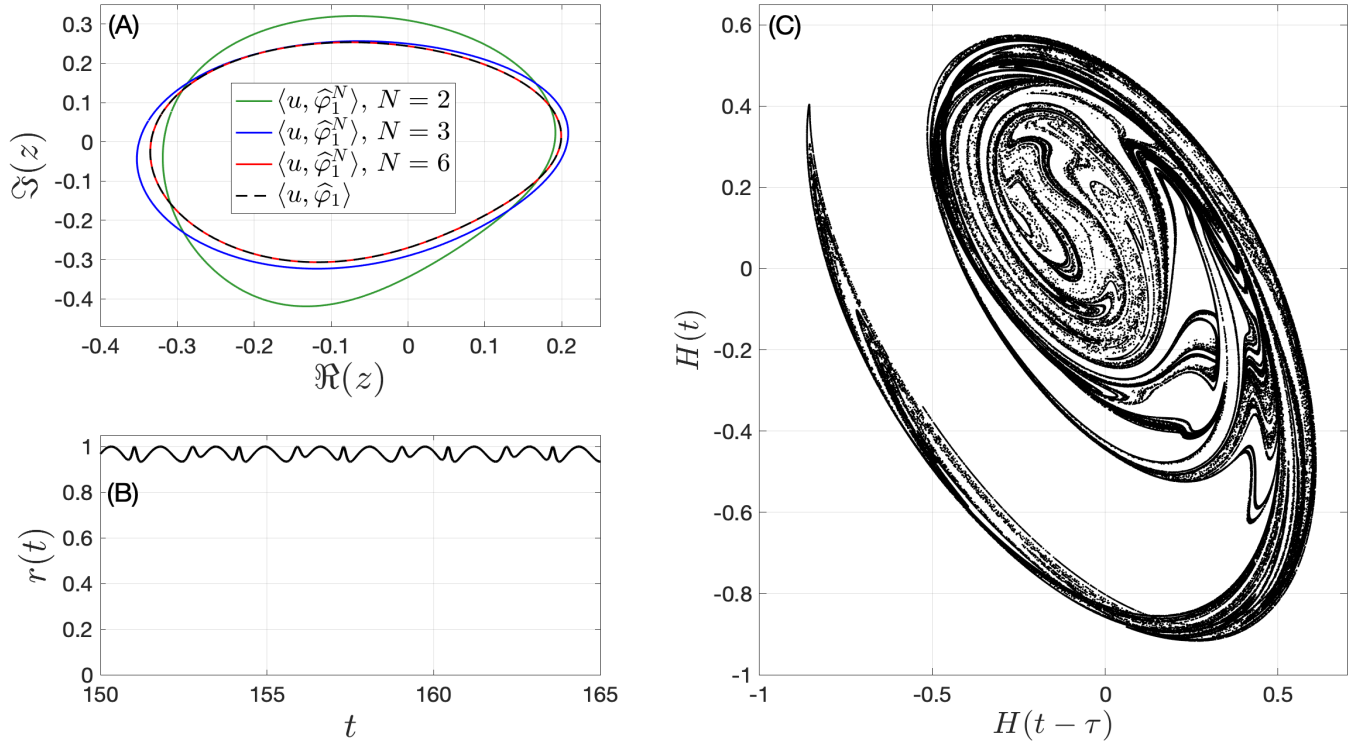

Supplementary Fig. 6: **Weak convergence of $\widehat{\varphi}_1^N$ towards $\widehat{\varphi}_1$; order parameter $r(t)$; and a snapshot attractor exhibiting horseshoes from Eq. (S21).** (**A**) Numerical illustration of the weak convergence of $\widehat{\varphi}_1^N$ towards $\widehat{\varphi}_1$. Here is shown the convergence of $\langle u(t), \widehat{\varphi}_1^N\rangle$ towards $\langle u(t), \widehat{\varphi}_1\rangle$ when $u(t)$ is the limit cycle of the KTF model, i.e. for the unperturbed dynamics. This convergence is quick: for $N = 6$ the precision is already of order 10^{-5}. (**B**) Order parameter $r(t)$ as computed from (S24). It shows that $\hat{z}_1 = \langle u, \widehat{\varphi}_1\rangle$ and $z_1 = \langle u, \varphi_1\rangle$ evolve in a synchronous fashion in the course of time; see Text. (**C**) Snapshot attractor from Eq. (S21) in which $\langle u, \widehat{\varphi}_1\rangle$ has replaced $\langle u, \varphi_1\rangle$ used in the *Main Text*. Here 3.4×10^5 initial data are used to produce this snapshot.

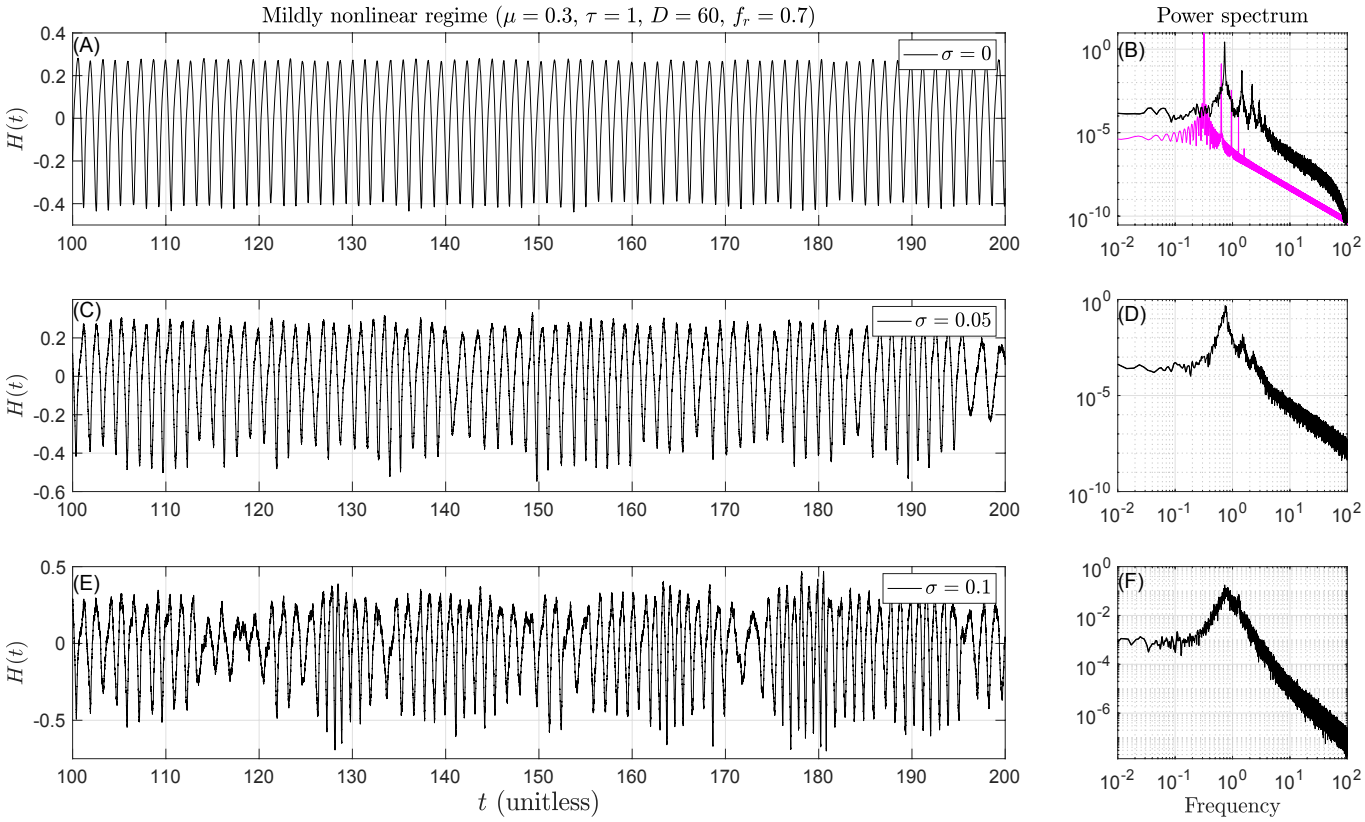

Supplementary Fig. 7: **Parameter dependence in σ for the mildly nonlinear regime, $\mu = 0.3$ and $\tau = 1$ (Regime A).** The magenta curve in (B) corresponds to the power spectrum of the periodic orbit for $D = \sigma = 0$. The case $\sigma = 0$ and $D \neq 0$ corresponds to a random periodic case. The cases $\sigma = 0.05$ and $\sigma = 0.1$ to noise-driven solutions evolving on a random chaotic attractor exhibiting stretching and folding (horseshoes). The case $\sigma = 0.1$ is shown in *Fig. 4 of the Main Text* but is reproduced here for the sake of comparison (with the time series in (E) shown over a longer time interval).

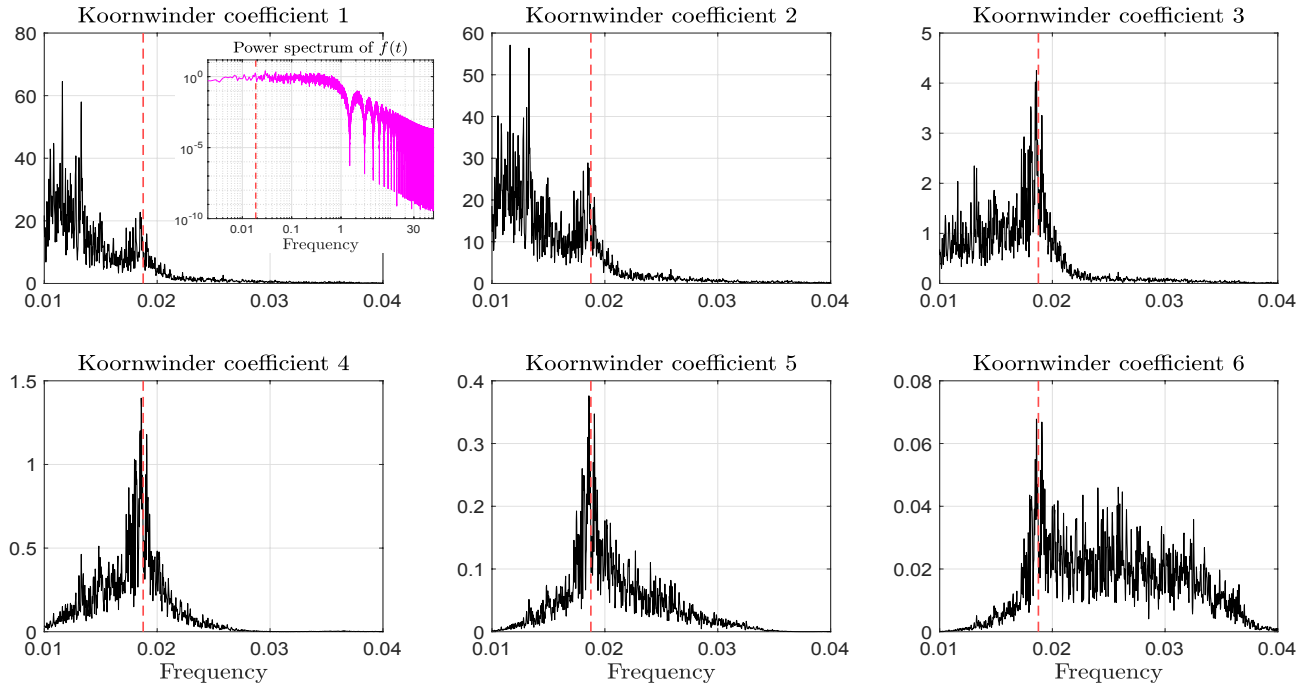

Supplementary Fig. 8: **Power spectra (linear scale) across a few Koornwinder coefficients together with the power spectrum of $f(t)$ shown in log-log scale.** In each panel, the vertical dashed red line marks the location of the second bump's dominant frequency as displayed by the noise-driven chaos time-series in *Fig. 8B (red curve) of the Main Text.*

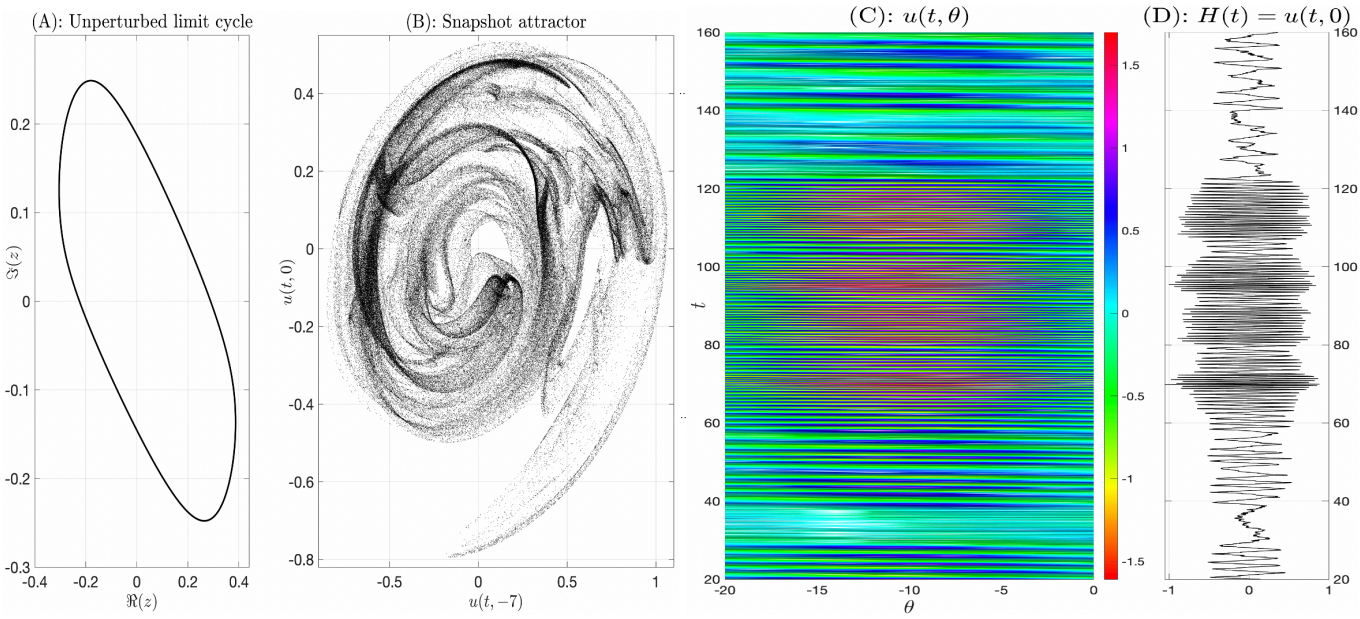

Supplementary Fig. 9: **Dynamics of the stochastic transport problem of the Main Text in a strongly nonlinear regime (Regime B)**. (**A**) 2-D projection onto the unstable mode φ_1 of the unperturbed KTF model's limit cycle in Regime B (i.e. for $\mu = 1.2$ and $\tau = 20$). (**B**) Strange snapshot attractor in Regime B. Here the snapshot attractor $\mathcal{A}(t)$, at a given time t, of the stochastic transport problem *Eqns. (9)-(10) from the Main Text* is shown in the reduced state space $(u(t,-7), u(t,0))$. We observe stretch-and-fold features embedded in a "foggier" background than for the snapshot attractors shown in *Figs. 3A and 3B of the Main Text*. The parameter values of the noise terms are here $D = 40$, $f_r = 0.7$ and $\sigma = 0.1$, i.e. those used for *Figs. 6E and 6F of the Main Text*. Here 2.5×10^5 initial data are used to produce this snapshot. (**C**) shows a solution $u(t,\theta)$ to the associated stochastic transport problem *Eqns. (9)-(10) from the Main Text*, and its boundary value $u(t,0)$ at $\theta = 0$, providing a stochastic path $H(t)$ shown in (**D**).

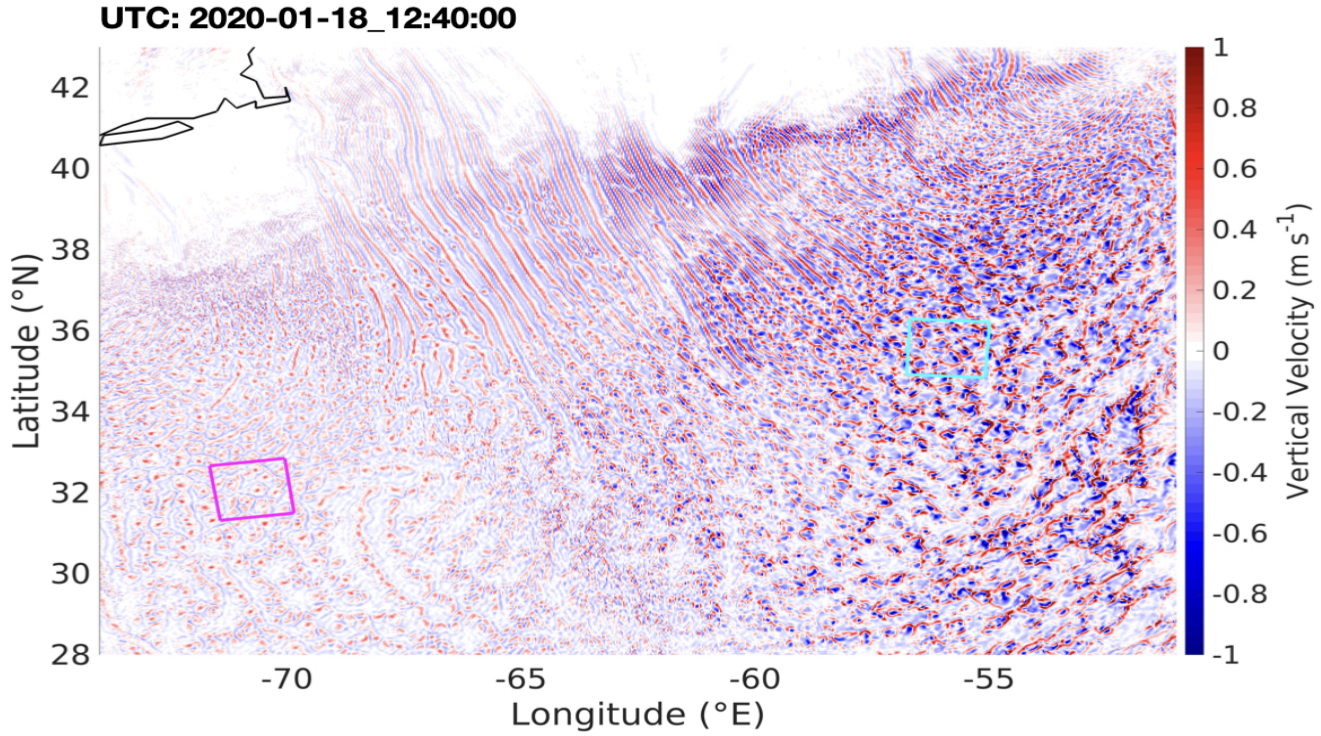

Supplementary Fig. 10: **A snapshot of the vertical velocity field as modeled by the WRF model**. The field is shown at the same specific time (January 18, 2020, UTC 12:40:00) for the same domain as shown in Fig. 1A of the Main Text. The magenta and cyan boxes correspond to (C) and (B) of Fig. 1of the Main Text, respectively. See Main Text for more details.

Supplementary movie files

We provide three supplementary movie files to show the time-evolution of snapshot attractors for three different settings corresponding respectively to the snapshot attractors shown in Fig. 3 (A and B) *of the Main Text*, Fig. 3 (C and D) *of the Main Text*, and Supplementary Fig. 9B.

- **Supplementary Movie 1**: Time-evolution of snapshot attractors obtained from the stochastic transport problem *(9)-(10) of the Main Text* for Regime A (horseshoes case).
- **Supplementary Movie 2**: Time-evolution of snapshot attractors obtained from the stochastic transport problem (**S17**)-(**S19**) (murmuration case).
- **Supplementary Movie 3**: Time-evolution of snapshot attractors obtained from the stochastic transport problem *(9)-(10) of the Main Text* for Regime B; i.e. the case shown in Supplementary Fig. 9.

REFERENCES AND NOTES

1. B. Van der Pol, J. Van Der Mark, Frequency demultiplication. *Nature*, **120**, 363–364 (1927).

2. L.-S. Young, Generalizations of SRB measures to nonautonomous, random, and infinite dimensional systems. *J. Stat. Phys.* **166**, 494–515 (2017).

3. J. Guckenheimer, M. Wechselberger, L.-S. Young, Chaotic attractors of relaxation oscillators. *Nonlinearity* **19**, 701–720 (2006).

4. M. D. Chekroun, E. Simonnet, M. Ghil, Stochastic climate dynamics: Random attractors and time-dependent invariant measures. *Physica D* **240**, 1685–1700 (2011).

5. T. Bódai, G. Károlyi, T. Tél, A chaotically driven model climate: Extreme events and snapshot attractors. *Nonl. Proc. Geophys.* **18**, 573–580 (2011).

6. Q. Wang, L.-S. Young. Strange attractors in periodically-kicked limit cycles and Hopf bifurcations. *Commun. Math. Phys.* **240**, 509–529 (2003).

7. Q. Wang, L.-S. Young, Strange attractors with one direction of instability. *Commun. Math. Phys.* **218**, 1–97 (2001).

8. Q. Wang, L.-S. Young. Toward a theory of rank one attractors. *Ann. Math.* **167**, 349–480 (2008).

9. S. Wieczorek. Stochastic bifurcation in noise-driven lasers and Hopf oscillators. *Phys. Rev. E* **79**, 036209, 2009.

10. K. C. A. Wedgwood, K. K. Lin, R. Thul, S. Coombes. Phase-amplitude descriptions of neural oscillator models. *J. Math. Neurosci.* **3**, 2 (2013).

11. P. Ashwin, S. Coombes, R. Nicks. Mathematical frameworks for oscillatory network dynamics in neuroscience. *J. Math. Neurosci.* **6**, 2 (2016).

12. K. K. Lin, L.-S. Young, Shear-induced chaos. *Nonlinearity* **21**, 899 (2008).

13. K. Lu, Q. Wang, L.-S. Young. *Strange Attractors for Periodically Forced Parabolic Equations*, volume 224 of *Memoirs of the American Mathematical Society* (American Mathematical Society, Providence, RI, 2013).

14. G. A Bocharov, F. A. Rihan, Numerical modelling in biosciences using delay differential equations. *J. Comp. Appl. Math.* **125**, 183–199 (2000).

15. J. D. Murray, *Mathematical Biology: I. An Introduction* (Springer, 2002).

16. K. Bansal, J. O. Garcia, S. H. Tompson, T. Verstynen, J. M. Vettel, S. F. Muldoon. Cognitive chimera states in human brain networks. *Sci. Adv.* **5**, eaau8535 (2019).

17. A. Arenas, A. Díaz-Guilera, J. Kurths, Y. Moreno, C. Zhou, Synchronization in complex networks. *Phys. Rep.* **469**, 93–153 (2008).

18. M. C. Soriano, J. García-Ojalvo, C. R. Mirasso, I. Fischer. Complex photonics: Dynamics and applications of delay-coupled semiconductors lasers. *Rev. Mod. Phys.* **85**, 421–470 (2013).

19. N. Boers, M. D. Chekroun, H. Liu, D. Kondrashov, D.-D. Rousseau, A. Svensson, M. Bigler, M. Ghil, Inverse stochastic–dynamic models for high-resolution Greenland ice core records. *Earth Syst. Dynam.* **8**, 1171–1190 (2017).

20. A. Keane, B. Krauskopf, C. M. Postlethwaite, Climate models with delay differential equations. *Chaos* **27**, 114309 (2017).

21. S. K. J. Falkena, C. Quinn, J. Sieber, J. Frank, H. A. Dijkstra, Derivation of delay equation climate models using the Mori-Zwanzig formalism. *Proc. R. Soc. A* **475**, 20190075 (2019).

22. K. Gopalsamy, *Stability and Oscillations in Delay Differential Equations of Population Dynamics* (Springer Science & Business Media, 2013), vol. 74.

23. T. Erneux, J. Javaloyes, M. Wolfrum, S. Yanchuk, Introduction to focus issue: Time-delay dynamics. *Chaos* **27**, 114201 (2017).

24. H. Wernecke, B. Sándor, C. Gros, Chaos in time delay systems, an educational review. *Phys. Rep.* **824**, 1–40 (2019).

25. M. D. Chekroun, M. Ghil, J. D. Neelin, Pullback attractor crisis in a delay differential ENSO model, in *Advances in Nonlinear Geosciences*, A. Tsonis, Ed. ,(Springer, 2018), pp. 1–33.

26. T. Erneux, *Applied Delay Differential Equations* (Springer Science & Business Media, 2009), vol. 3.

27. K. D. Beheng, A parameterization of warm cloud microphysical conversion processes. *Atmos. Res.* **33**, 193–206 (1994).

28. J. W.-B. Lin, J. D. Neelin. Considerations for stochastic convective parameterization. *J. Atmos. Sci.* **59**, 959–975 (2002).

29. J. Berner, U. Achatz, L. Batte, L. Bengtsson, A. Cámara, H. M. Christensen, M. Colangeli, D. R. B. Coleman, D. Crommelin, S. I. Dolaptchiev, C. L. E. Franzke, P. Friederichs, P. Imkeller, H. Järvinen, S. Juricke, V. Kitsios, F. Lott, V. Lucarini, S. Mahajan, T. N. Palmer, Stochastic parameterization: Toward a new view of weather and climate models. *Bull. Am. Meteorol. Soc.* **98**, 565–588 (2017).

30. I. Koren, G. Feingold. Aerosol-cloud-precipitation system as a predator-prey problem. *Proc. Natl. Acad. Sci. U.S.A.* **108**, 12227–12232 (2011).

31. I. Koren, E. Tziperman, G. Feingold, Exploring the nonlinear cloud and rain equation. *Chaos* **27**, 013107 (2017).

32. M. D. Chekroun, I. Koren, H. Liu. Efficient reduction for diagnosing Hopf bifurcation in delay differential systems: Applications to cloud-rain models. *Chaos* **30**, 053130 2020.

33. H. Xue, G. Feingold, B. Stevens. Aerosol effects on clouds, precipitation, and the organization of shallow cumulus convection. *J. Atmos. Sci.* **65**, 392–406 (2008).

34. H. Wang, G. Feingold. Modeling mesoscale cellular structures and drizzle in marine stratocumulus. Part II: The microphysics and dynamics of the boundary region between open and closed cells. *J. Atmos. Sci.*, **66**, 3257–3275 (2009).

35. I. Koren, G. Feingold. Adaptive behavior of marine cellular clouds. *Sci. Rep.*, **3**, 2507 (2013).

36. S. Smale. Differentiable dynamical systems. *Bull. Am. Math. Soc.* **73**, 747–817 (1967).

37. J. Guckenheimer, P. Holmes, *Nonlinear Oscillations, Dynamical Systems, and Bifurcations of Vector Fields* (Springer Science & Business Media, 2013), vol. 42.

38. A. Cavagna, A. Cimarelli, I. Giardina, G. Parisi, R. Santagati, F. Stefanini, M. Viale. Scale-free correlations in starling flocks. *Proc. Natl. Acad. Sci. U.S.A.* **107**, 11865–11870 (2010).

39. T. J. Schmit, P. Griffith, M. M. Gunshor, J. M. Daniels, S. J. Goodman, W. J. Lebair. A closer look at the ABI on the GOES-R series. *Bull. Am. Meteorol. Soc.* **98**, 681–698 (2017).

40. S. Lunderman, M. Morzfeld, F. Glassmeier, G. Feingold. Estimating parameters of the nonlinear cloud and rain equation from a large-eddy simulation. *Physica D* **410**, 132500 (2020).

41. W. C. Skamarock, J. B. Klemp, J. Dudhia, D. O. Gill, Z. Liu, J. Berner, W. Wang, J. G. Powers, M. G. Duda, D. M. Barker, X.-Y. Huang, A description of the advanced research WRF model version 4. *National Center for Atmospheric Research (NCAR) Technical Notes*, TN-556+STR, 2021.

42. A. Winfree, Biological rhythms and the behavior of populations of coupled oscillators. *J. Theor. Biol.* **16**, 15–42 (1967).

43. A. Winfree, *The Geometry of Biological Time* (Springer-Verlag, Berlin, 1980).

44. E. A. Coddington, N. Levinson, *Theory of Ordinary Differential Equations* (Tata McGraw-Hill Education, 1955).

45. J. Guckenheimer, Isochrons and phaseless sets. *J. Math. Biol.* **1**, 259–273 (1975).

46. E. M. Izhikevich, *Dynamical Systems in Neuroscience: The Geometry of Excitability and Bursting* (MIT Press, 2010).

47. M. Engel, J. S. W. Lamb, M. Rasmussen. Bifurcation analysis of a stochastically driven limit cycle. *Commun. Math. Phys.* **365**, 935–942 (2019).

48. T. Son Doan, M. Engel, J. S. W. Lamb, M. Rasmussen, Hopf bifurcation with additive noise. *Nonlinearity*, **31**, 4567–4601 (2018).

49. J. M. Ottino, *The Kinematics of Mixing: Stretching, Chaos, and Transport* (Cambridge Univ. Press, 1989), vol. 3.

50. M. D. Chekroun, M. Ghil, H. Liu, S. Wang. Low-dimensional Galerkin approximations of nonlinear delay differential equations. *Discrete Continuous Dyn. Syst.* **36**, 4133–4177 (2016).

51. M. D. Chekroun, H. Liu, J. C. McWilliams, Variational approach to closure of nonlinear dynamical systems: Autonomous case. *J. Stat. Phys.* **179**, 1073–1160 (2020).

52. A. Tantet, M. D. Chekroun, H. A. Dijkstra, J. D. Neelin. Ruelle-Pollicott resonances of stochastic systems in reduced state space. Part II: Stochastic Hopf Bifurcation. *J. Stat. Phys.* **179**, 1403–1448 (2020).

53. H. C. Rodean, *Stochastic Lagrangian Models of Turbulent Diffusion* (Springer, 1996), vol. 45.

54. S. N. Stechmann, J. D. Neelin. A stochastic model for the transition to strong convection. *J. Atmos. Sci.* **68**, 2955–2970 (2011).

55. A. J. Majda, S. N. Stechmann. Stochastic models for convective momentum transport. *Proc. Natl. Acad. Sci. U.S.A.* **105**, 17614–17619 (2008).

56. B. Khouider, A. J. Majda, M. A. Katsoulakis. Coarse-grained stochastic models for tropical convection and climate. *Proc. Natl. Acad. Sci. U.S.A.* **100**, 11941–11946 (2003).

57. J. Dorrestijn, D. T. Crommelin, A. P. Siebesma, H. J. J. Jonker, F. Selten. Stochastic convection parameterization with Markov chains in an intermediate-complexity GCM. *J. Atmos. Sci.* **73**, 1367–1382 (2016).

58. N. Chen, A. J. Majda, C. T. Sabeerali, R. S. Ajayamohan. Predicting monsoon intraseasonal precipitation using a low-order nonlinear stochastic model. *J. Climate*, **31**, 4403–4427 (2018).

59. A. Bellen, M. Zennaro, *Numerical Methods for Delay Differential Equations* (Oxford Univ. Press, 2013).

60. S. Maset. Numerical solution of retarded functional differential equations as abstract Cauchy problems. *J. Comput. Appl. Math.* **161**, 259–282 (2003).

61. A. Bellen, S. Maset. Numerical solution of constant coefficient linear delay differential equations as abstract Cauchy problems. *Numer. Math.* **84**, 351–374 (2000).

62. S. Yanchuk, G. Giacomelli, Spatio-temporal phenomena in complex systems with time delays. *J. Phys. A Math. Theor.* **50**, 103001 (2017).

63. F. T. Arecchi, G. Giacomelli, A. Lapucci, R. Meucci. Two-dimensional representation of a delayed dynamical system. *Phys. Rev. A*, **45**:R4225–R4228 (1992).

64. H. Aref. Stirring by chaotic advection. *J. Fluid Mech.*, **143**, 1–21 (1984).

65. J. M. Ottino, S. C. Jana, V. S. Chakravarthy. From Reynolds's stretching and folding to mixing studies using horseshoe maps. *Phys. Fluids*, **6**:685–699, 1994.

66. K. Wójcik, P. Zgliczyński. Topological horseshoes and delay differential equations. *Discrete Continuous Dyn. Syst.* **12**, 827–852 (2005).

67. C. Feng, H. Zhao. Random periodic processes, periodic measures and ergodicity. *J. Differ. Equ.* **269**, 7382–7428 (2020).

68. O. E. Rossler, An equation for hyperchaos. *Phys. Lett. A* **71**, 155–157 (1979).

69. G. Baier, S. Sahle, Design of hyperchaotic flows. *Phys. Rev. E* **51**, R2712–R2714 (1995).

70. M. D. Chekroun, J. D. Neelin, D. Kondrashov, J. C. McWilliams, M. Ghil. Rough parameter dependence in climate models and the role of Ruelle-Pollicott resonances. *Proc. Natl. Acad. Sci. U.S.A.*, **111**, 1684–1690 (2014).

71. M. D. Chekroun, A. Tantet, H. A. Dijkstra, J. D. Neelin. Ruelle–Pollicott resonances of stochastic systems in reduced state space. Part I: Theory. *J. Stat. Phys.* **179**, 1366–1402 (2020).

72. T. Dror, V. Silverman, O. Altaratz, M. D. Chekroun, I. Koren, Uncovering the large-scale meteorology that drives continental, shallow, green cumulus through supervised classification. *Geophys. Res. Lett.* **49**, e2021GL096684 (2022).

73. R. Wood. Stratocumulus clouds. *Mon. Weather Rev.*, **140**:2373–2423, 2012.

74. A. Guillamon, G. Huguet. A computational and geometric approach to phase resetting curves and surfaces. *SIAM J. Appl. Dyn. Syst.* **8**, 1005–1042 (2009).

75. A. Mauroy, B. Rhoads, J. Moehlis, I. Mezic. Global isochrons and phase sensitivity of bursting neurons. *SIAM J. Appl. Dyn. Syst.* **13**, 306–338 (2014).

76. M. Detrixhe, M. Doubeck, J. Moehlis, F. Gibou. A fast Eulerian approach for computation of global isochrons in high dimensions. *SIAM J. Appl. Dyn. Syst.* **15**, 1501–1527 (2016).

77. M. J. Panaggio, D. M. Abrams. Chimera states: Coexistence of coherence and incoherence in networks of coupled oscillators. *Nonlinearity* **28**, R67 (2015).

78. J. M. Gomes, R. Weber dos Santos, E. M. Cherry. Alternans promotion in cardiac electrophysiology models by delay differential equations. *Chaos* **27**, 093915 (2017).

79. K. H. W. J. ten Tusscher, D. Noble, P.-J. Noble, A. V. Panfilov. A model for human ventricular tissue. *Am. J. Physiol. Heart Circ. Phys.* **286**, H1573–H1589 (2004).

80. J. E. Marsden, M. McCracken, *The Hopf Bifurcation and Its Applications* (Springer Science & Business Media, 2012), vol. 19.

81. T. Ma, S. Wang. *Phase Transition Dynamics* (Springer, 2014).

82. D. Kondrashov, M. D. Chekroun, P. Berloff. Multiscale Stuart-Landau emulators: Application to wind-driven ocean gyres. *Fluids* **3**, 21, (2018).

83. M. D. Chekroun, H. Liu, J. C. McWilliams. Stochastic rectification of fast oscillations on slow manifold closures. *Proc. Natl. Acad. Sci. U.S.A.*, **118**, e2113650118 (2021).

84. G. Thompson, T. Eidhammer. A study of aerosol impacts on clouds and precipitation development in a large winter cyclone. *J. Atmos. Sci.*, **71**, 3636–3658 (2014).

85. S.-Y. Hong, Y. Noh, J. Dudhia. A new vertical diffusion package with an explicit treatment of entrainment processes. *Mon. Weather Rev.* **134**, 2318–2341 (2006).

86. P. A. Jiménez, J. Dudhia, J. F. González-Rouco, J. Navarro, J. P. Montávez, E. García-Bustamante. A revised scheme for the WRF surface layer formulation. *Mon. Weather Rev.* **140**, 898–918 (2012).

87. K. Engelborghs, T. Luzyanina, D. Roose. Numerical bifurcation analysis of delay differential equations using DDE-BIFTOOL. *ACM Trans. Math. Softw.* **28**, 1–21 (2002).

88. R. B. Vinter, On the evolution of the state of linear differential delay equations in M^2: Properties of the generator. *IMA J. Appl. Math.* **21**, 13–23, 1978.